Acta Materialia 280 (2024) 120335

Contents lists available at ScienceDirect

Acta Materialia

journal homepage: www.elsevier.com/locate/actamat

Full length article

Hydrogen-enhanced microbanding in an austenitic FeMnAlC low-density steel: Effect on hydrogen embrittlement resistance

Ivan Gutierrez-Urrutia *, Yuhei Ogawa, Akinobu Shibata

Research Center for Structural Materials, National Institute for Materials Science (NIMS), 1-2-1, Sengen, Tsukuba 305-0047, Japan.

ARTICLE INFO

Keywords:
FeMnAlC low-density steels
Hydrogen embrittlement
Strain localization
Microbands
Deformation bands
Electron channeling contrast imaging

ABSTRACT

We have investigated the influence of 101 mass ppm hydrogen content on the room temperature deformation structure and mechanical behavior of an austenitic Fe30Mn6.5Al0.3C (wt.%) low-density steel by several electron microscopy techniques, such as electron channeling contrast imaging (ECCI), electron backscatter diffraction (EBSD), and scanning transmission electron microscopy (STEM). The steel exhibits a high hydrogen embrittlement resistance associated with a moderated increase in strength (yield stress increase of 10%) and ductility (increase in the elongation to fracture of ~ 8%). Analysis of the deformation structure reveals that hydrogen influences the deformation behavior by promoting deformation mechanisms associated with inhomogeneous plasticity (hydrogen-enhanced deformation banding (HEDB)) and strain localization (hydrogen-enhanced microbanding (HEMB)). These deformation mechanisms are ascribed to hydrogen-induced effects on dislocation plasticity, resulting in macroscopic kink bands, sub-micron localized strain gradients, and localized shear at cell blocks. We find that HEMB plays a relevant role in the deformation behavior of sub-micron localized strain gradients by promoting plastic relaxation and the enhanced storage of geometrically necessary dislocations within them. These effects mitigate the activation of damage mechanisms and enhance the strain-hardening capacity, contributing to the high HE resistance of the steel, comparable to that of high HE-resistant fcc alloys and steels.

1. Introduction

FeMnAlC low-density steels are an attractive alloy class for structural components in the automotive and aircraft industry [1–3]. The high Al content (5 – 11 wt.%) offers substantial weight saving while keeping a superior strength and ductility balance [1]. This effect allows for a mass reduction of more than 30% when used in safety-critical vehicle parts [2]. Interestingly, these steels offer a high tunability of the mechanical properties due to the wide compositional range of the main structural phases, namely, fcc (austenite), bcc (ferrite), and $L1_2$-type phase (κ-carbides). When exposed to hydrogen, FeMnAlC low-density steels have a potential good hydrogen embrittlement (HE) resistance due to the high aluminum content. This element in solid solution has the following influence on these steels: reduces the strain aging caused by carbon [2]; reduces the twinning activity due to the increased stacking fault energy (SFE), limiting the activation of quasi-cleavage fracture induced by twin-GB interactions [3-5]; reduces hydrogen diffusivity due to the atomic trapping mechanism [6]; and limits the hydrogen permeability due to the formation of a surface Al_2O_3 layer [7]. Among the different classes of FeMnAlC low-density steels, mechanically stable austenitic steels offer superior HE resistance due to the suppression of the structural phases α' (bcc)-martensite, ε (hcp)-martensite, and ordered ($L1_2$-type) κ-carbides that have detrimental effects on the hydrogen-assisted fracture behavior [8-12].

So far, the underlying dislocation-based mechanisms controlling hydrogen-induced effects on plasticity in austenitic FeMnAlC low-density steels are unknown. In austenitic steels exhibiting a strong planar slip, hydrogen-induced strain localization effects associated with the formation of coarse slip bands and deformation bands (DBs) have been reported [13-16]. These studies show that hydrogen-induced strain localization tends to promote an early material failure and, hence, ductility degradation, due to grain boundary cracking via slip band-assisted void formation and coalescence along grain boundaries. Our recent studies [17,18] have shown that austenitic FeMnAlC low-density steels exhibit strain localization associated with intense shear localization due to microbanding, which may lead to ductility degradation when these steels are exposed to hydrogen. On the other hand, recent studies have shown that hydrogen modifies several features

* Corresponding author.
E-mail address: gutierrezurrutia.Ivan@nims.go.jp (I. Gutierrez-Urrutia).

https://doi.org/10.1016/j.actamat.2024.120335
Received 4 April 2024; Received in revised form 22 August 2024; Accepted 23 August 2024
Available online 26 August 2024

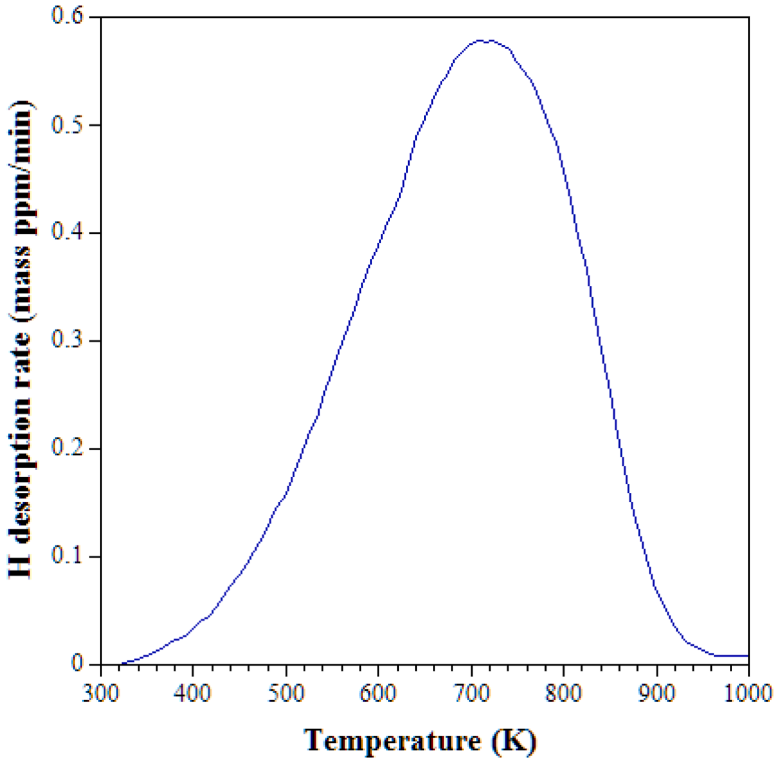

Figure 1. Hydrogen desorption curve of the hydrogen-charged sample. The total measured hydrogen concentration was 101 mass ppm.

of the dislocation and twin structures in highly ductile fcc materials, such as dislocation cell size, cell block size, dislocation density at cell walls, and twinning stress [19-25]. These phenomena have been ascribed to several hydrogen-induced effects, namely, the elastic shielding of the strain field associated with dislocations [23,26-28], reduction of the constriction energy of extended dislocations [29,30], and reduction in stacking fault energy (SFE) [23-25,31]. Although the influence of the above-described hydrogen-induced effects on the deformation and mechanical behavior of fcc alloys is still under debate, recent studies have demonstrated the potential use of the hydrogen-induced reduction on SFE to design multicomponent fcc alloys, such as FeCrNiMnCo and CoCrFeMnNi high-entropy alloys, and CoNiV medium-entropy alloys, with high HE resistance [32-35]. The hydrogen-enhanced activation of nano-twins in these alloys (hydrogen-enhanced densified twinning effect [36]), enhances the strain-hardening capacity, resulting in a high HE resistance. These studies have demonstrated that implementing hydrogen-induced effects on plasticity to alloy design approaches can lead to novel high HE-resistant fcc alloys.

Due to the current technological interest in FeMnAlC low-density steels as structural materials, the investigation of hydrogen-induced effects on the deformation behavior and strain localization phenomena of these steels can provide further insight into their mechanical behavior when exposed to hydrogen. For this goal, we have investigated the effect of hydrogen on the dislocation structure and its contribution to the mechanical behavior of an austenitic Fe30Mn6.5Al0.3C (wt.%) low-density steel by several electron microscopy techniques, such as electron channeling contrast imaging (ECCI), electron backscatter diffraction (EBSD), and scanning transmission electron microscopy (STEM). We selected this steel composition as an example of austenitic FeMnAlC steel free of kappa-carbides with a high weight reduction (~8.5% density reduction) [1]. The influence of hydrogen on the main characteristics of the different types of dislocation structures in the main texture components, namely <1 1 1>//tensile axis directions, <0 0 1>//tensile axis directions, and along the crystallographic line [1 1 2] – [1 0 1]//tensile axis was quantitatively analyzed. The contributions of the hydrogen-induced dislocation structure to the deformation behavior and mechanical properties were evaluated. Hydrogen-induced deformation mechanisms that can potentially enhance the HE resistance of the steel are discussed.

2. Materials and methods

The low-density steel investigated in the present study had the chemical composition Fe30Mn6.5Al0.3C (wt. %). Details of material processing can be found in [17]. The annealed material contains a fully austenitic structure with an average grain size of 175 μm, which remained stable at room temperature. Cylindrically shaped specimens of 6 mm in diameter and 30 mm in gage length were machined from the annealed plates along the rolling direction. The sample surface was mirror-finished by polishing with 1 μm diamond suspension. Tensile tests were performed at an initial strain rate of 5.0×10^{-5} s^{-1} in laboratory air at 295 K, using a screw-driven electromechanical test frame, Shimadzu AGX-plus, with 100 kN load capacity. The elongation of the gage part of the tensile specimen was measured by a contact-type strain gage extensometer. Two tensile experiments per condition (uncharged and hydrogen-charged) were performed to validate the mechanical tests. Both sets of tensile tests exhibited the mechanical behavior shown in Fig. 2. Central sections of the cylindrical-shaped samples cut along the tensile axis were analyzed to avoid surface effects associated with deformation constraints and hydrogen gradients on the deformation structure. The deformation structure was characterized by several electron microscopy techniques, such as electron channeling contrast imaging (ECCI), electron backscatter diffraction (EBSD), and scanning transmission electron microscopy (STEM). The SEM techniques (ECCI and EBSD) were performed in a Sigma Zeiss FEG-SEM and an Auriga Zeiss FI-SEM (Carl Zeiss SMT AG, Germany) equipped with Orientation Imaging Microscopy (OIM) EBSD systems. EBSD measurements were performed at 20 kV acceleration voltage, 15 - 20 mm working distance, and a step size of 50 – 100 nm. ECCI was conducted at 15 - 20 kV using a

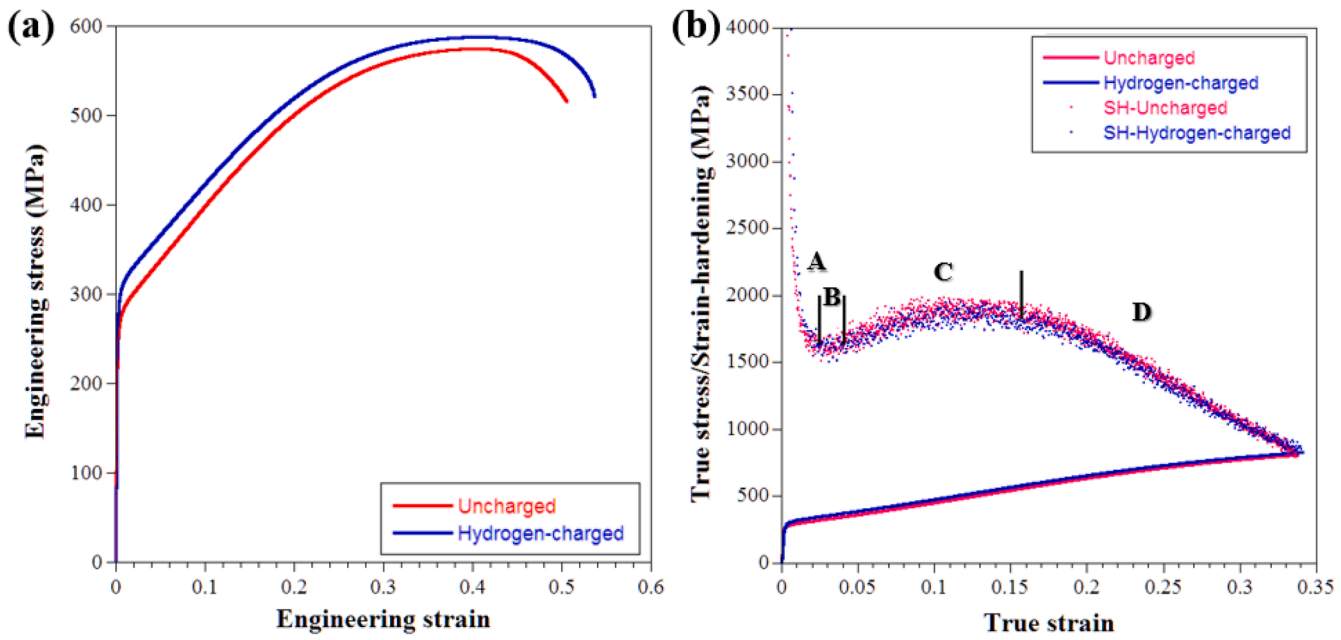

Figure 2. (a) Engineering stress-strain, (b) true stress-strain, and corresponding strain-hardening (SH) curves of uncharged and hydrogen-charged (101 mass ppm) Fe30Mn6.5Al0.3C (wt.%) low-density steel. Tensile tests were carried out at an initial strain rate of 5.0×10^{-5} s^{-1} in laboratory air at 295 K. Strain-hardening stages A, B, C, and D are described in the text.

Table 1
Effect of solute hydrogen (101 mass ppm) on the mechanical properties of a Fe-30Mn-6.5Al-0.3C (wt.%) low-density steel tested at 295 K. YS: Yield strength; UTS: Ultimate tensile strength; TFS: True fracture stress; UEL: Uniform elongation; ETF: Elongation-to-failure.

	YS (MPa)	UTS (MPa)	TFS (MPa)	UEL	ETF
Uncharged	275 ± 10	580 ± 5	825 ± 15	0.43 ± 0.01	0.51 ± 0.01
Hydrogen-charged	302 ± 10	595 ± 10	845 ± 15	0.46 ± 0.02	0.55 ± 0.01

solid-state four-quadrant backscatter electron (BSE) detector at a 6 – 7 mm working distance. The microscope was run in the high-current mode. ECC images were acquired by the EBSD-based ECCI approach described in [37,38]. ECCI samples were mechanically polished with 800 and 1200 SiC grit papers and subsequently polished with 9 and 3 μm diamond suspensions. Final polishing was performed with 250 nm colloidal silica suspension (Struers, OP-S). Tilting experiments were carried out on a 5-axis motorized eucentric stage (x, y, z, tilt, rotation) with x/y/z step resolution of 1 μm and tilt/rotation step resolution of 0.1°. STEM was performed in a JEOL JEM 2800 TEM operating at 200 kV. STEM samples were fabricated in areas of interest by the in-situ FIB lift-out method in a Scios 2 ThermoFisher Scientific dual-beam SEM

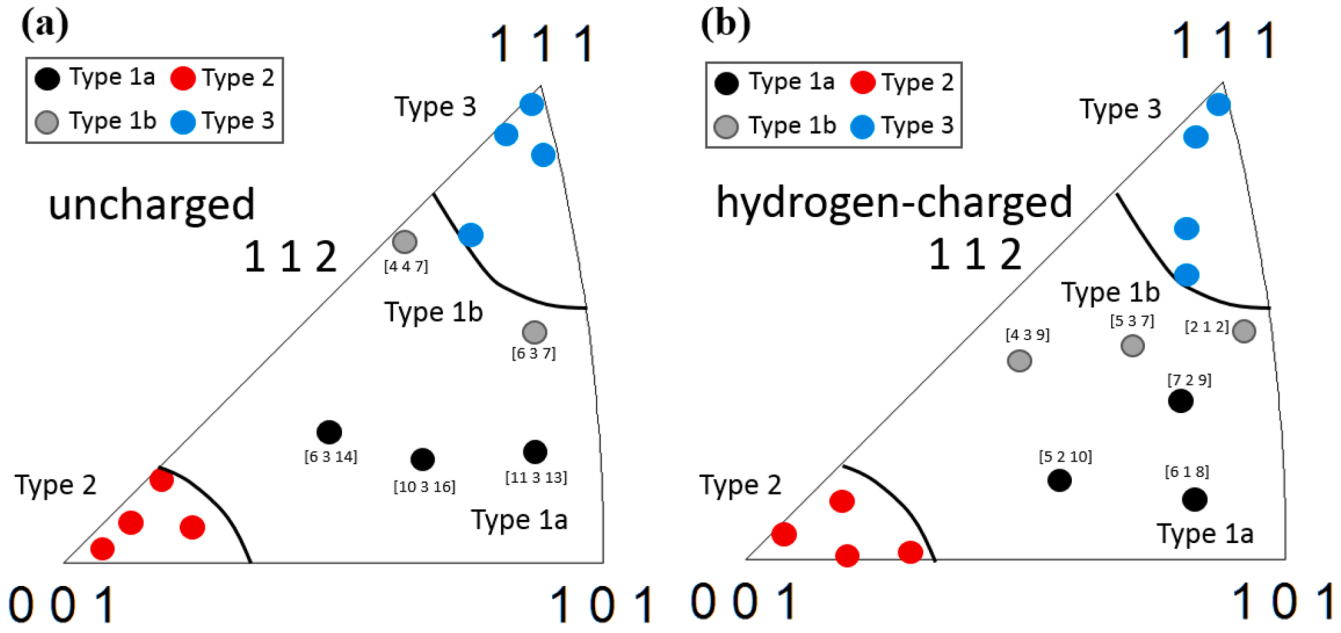

Figure 3. Inverse pole figures along the tensile axis direction of the grain orientations investigated in the uncharged sample (a) and hydrogen-charged sample (b). Grain orientations are classified according to the dislocation structures shown in Figs. 4, 5.

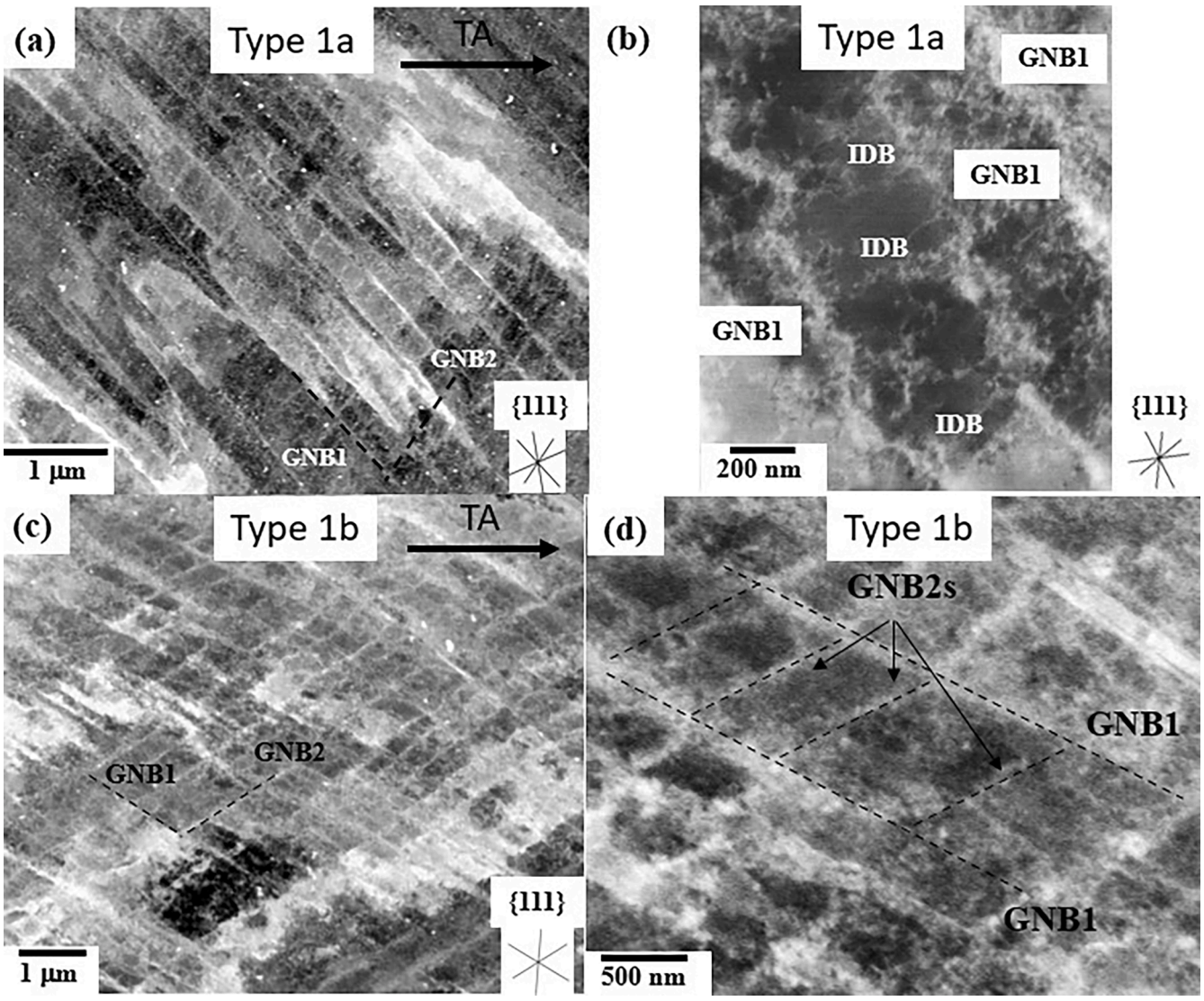

Figure 4. Classification of the dislocation structure in the uncharged sample. (a, b): Type 1a dislocation structure; (c, d): Type 1b dislocation structure. Grain orientations forming Type 1a and Type 1b dislocation structures are shown in Fig. 3. GNB: geometrically necessary boundary; IDB: incidental dislocation boundary. TA: tensile axis.

system. The observation plane of the STEM samples is the same as that used in ECCI. The thinning of the FIB lamella was performed at an initial acceleration voltage of 30kV and a milling current of ~1000 pA on both sides of the sample followed by a final thinning procedure at 5 kV and 200 pA to avoid surface damage induced by FIB milling [39]. No radiation damage (point defects or Ga-rich precipitates) was observed during STEM observations.

The hydrogen charging process was performed before the tensile tests by exposing the tensile specimens to a pressurized gaseous hydrogen environment of 100 MPa and 543 K for 200 h in an autoclave. This charging condition was determined so that the distribution of hydrogen content in the gage part of tensile specimens becomes uniform. After the tensile testing, solute hydrogen concentration was measured by gas chromatography thermal desorption analysis (TDA) with a thermal conductivity detector at a heating rate of 100 K/h. A cylindrical sample with a 5 mm height was cut from the uniformly deformed part of the fractured specimen for TDA. Fig. 1 shows the TDA curve of the hydrogen-charged specimen. The curve shows only one peak corresponding to lattice diffusion. The measured hydrogen concentration was 101 mass ppm. Since the hydrogen charging was performed before the tensile tests, we consider that the hydrogen content in the specimen is nearly constant during the tensile test. The estimated hydrogen concentration in the uncharged sample is < 5 mass ppm.

3. Results

3.1. Mechanical behavior

Fig. 2 shows the engineering (a) and true (b) stress-strain curves of the uncharged and hydrogen-charged samples tested at 295 K. The corresponding variation of the strain-hardening with true strain is plotted in (b). The plots show that solute hydrogen increases the yield stress (YS), flow stress (FS), ultimate tensile strength (UTS), uniform elongation (UEL), and elongation-to-failure (ETF) of the steel. In particular, the hydrogen-induced increase in YS is comparatively higher than that on the flow stress. Specifically, the increase on YS is ~ 27 MPa, and that on FS is between 14 MPa ($\varepsilon = 0.4$) and 25 MPa ($\varepsilon = 0.1$). These results indicate that the hardening effect of hydrogen on YS is higher than on FS. Interestingly, the present low-density steel exhibits a moderated increase in ductility when exposed to hydrogen. UEL and ETF increased from 0.43 ± 0.01 to 0.46 ± 0.02 and from 0.51 ± 0.01 to 0.55 ± 0.01, respectively. Table 1 summarizes the influence of hydrogen on

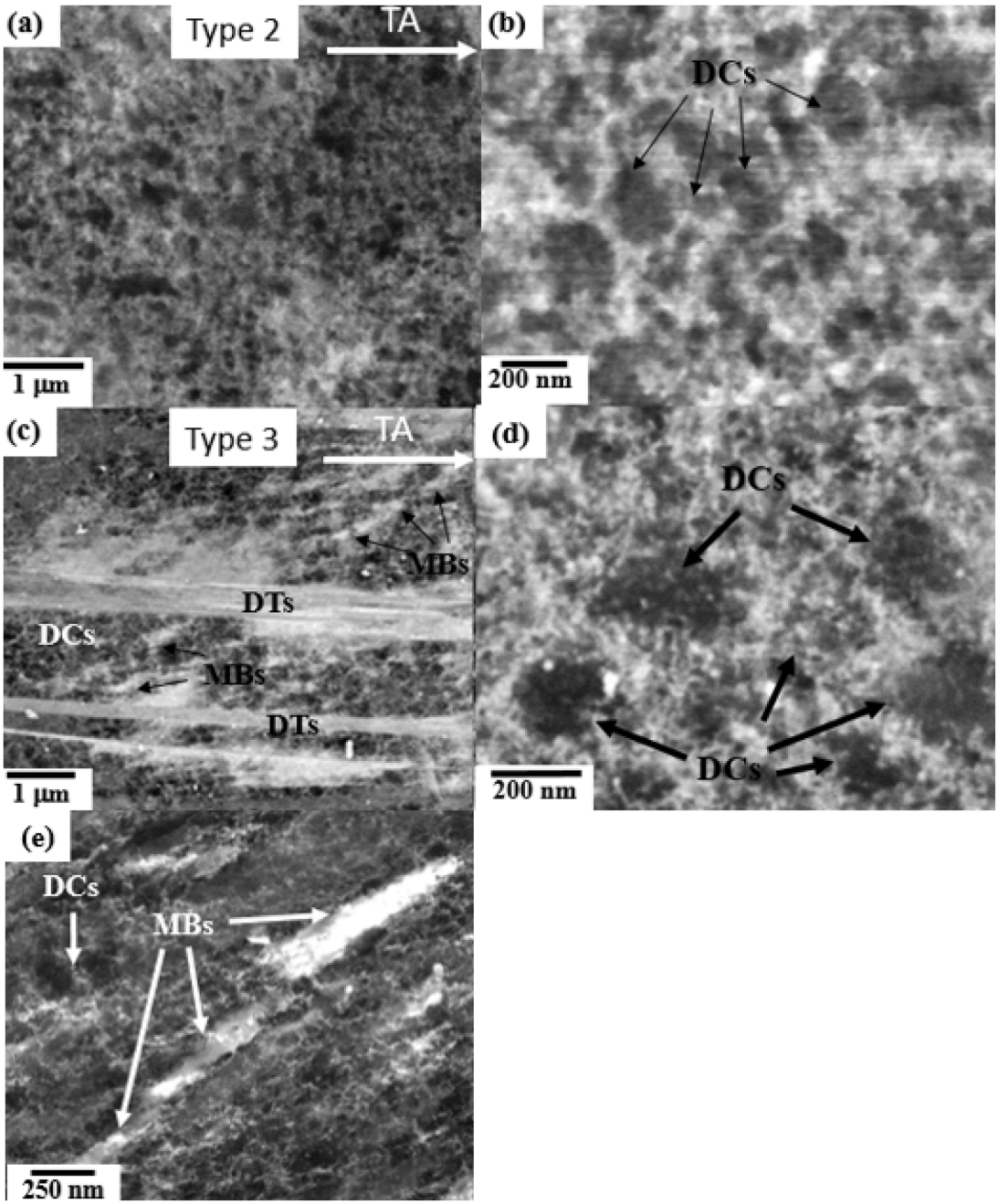

Figure 5. Classification of the dislocation structure in the uncharged sample. (a, b): Type 2 dislocation structure; (c - e): Type 3 dislocation structure. Grain orientations forming Type 2 and Type 3 dislocations structures are shown in Fig. 3. DCs: Dislocation cells; DTs: deformation twins; MBs: Microbands; DDWs: Dense dislocation walls. TA: tensile axis.

the mechanical properties.

Fig. 2(b) shows that both uncharged and hydrogen-charged samples exhibit similar strain-hardening behavior, with four hardening stages (A-D). The first stage (Stage A) is close to the Stage III hardening regime of fcc metals having a high SFE [40,41] and is characterized by a continuous decrease in the strain-hardening rate. Stage B reveals a constant hardening rate, which indicates the activation of a strain-hardening mechanism. With further straining, the strain-hardening rate increases gradually, reaching a plateau at $\varepsilon = 0.11$ (Stage C), and subsequently decreases until rupture (Stage D). Our former study [18] has shown that the strain-hardening of the uncharged Fe30Mn6.5Al0.3C steel is mainly associated with the evolution of the dislocation structure, namely dislocation cells and cell blocks, with straining. The relatively high SFE at 293K (SFE $= 64 \pm 10$ mJ/m^2 [18]) postpones the activation of deformation twinning to the later deformation stages, limiting its contribution to strain-hardening. Fig. 2(b) shows that the strain-hardening curve of the hydrogen-charged sample is similar to that of the uncharged sample. No extra hardening stage associated with deformation twinning is observed.

3.2. *Influence of hydrogen on the dislocation structure*

The dislocation structures of the uncharged and hydrogen-charged samples formed at the end of the uniform deformation stage ($\varepsilon = 0.4$) were evaluated on the main components of the tensile deformation texture, namely <0 0 1>//TA, <1 1 1>//TA, and along the crystallographic line [1 1 2] – [1 0 1]//TA (TA: tensile axis). The grain orientations evaluated in the uncharged and hydrogen-charged samples are

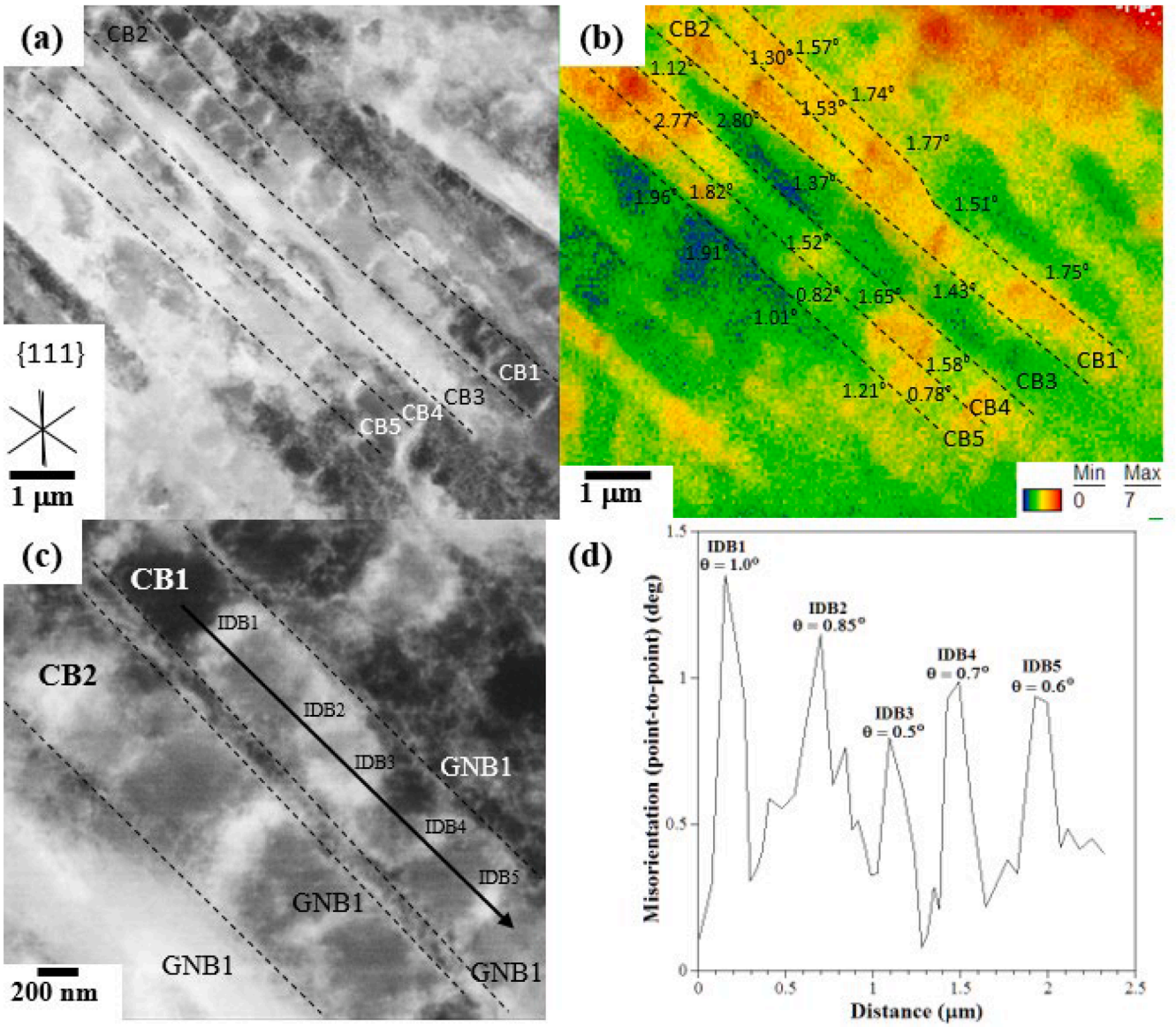

Figure 6. Combined ECCI and EBSD analysis of GNB/IDB misorientations in Type 1a CBs. (a): ECC image; (b): Grain reference orientation deviation EBSD map (reference point was set as the point in the map with the lowest kernel average misorientation); (c, d): Evaluation of IDB misorientations by EBSD misorientation profile analysis along the interior of CB1.

plotted in Fig. 3. About 13 - 14 grain orientations per sample were evaluated. Following our ECCI analysis on the dislocation structure formed in the tensile deformed uncharged sample [18] and former studies on the grain orientation dependence of the dislocation structure formed under tensile deformation conditions in fcc metals [42-45], we classify the dislocation structure with respect to the grain orientation as follows (Figs. 4, 5). Type 1 dislocation structure consists of a cell block (CB) structure delimited by geometrically necessary boundaries (GNBs) and incidental dislocation boundaries (IDBs). This dislocation structure is formed in grains oriented along the crystallographic line [1 1 2] – [1 0 1]//TA. Two main slip classes are active in the analyzed grain orientations: single slip (primary slip system) and two-fold slip (two non-coplanar slip systems). Accordingly, we subdivide the CB structure into two classes, namely Type 1a and Type 1b, to account for the effect of the slip class. Type 1a CBs are characterized by a primary GNB system (GNB1 in Figs. 4(a, b)), a secondary GNB system (GNB2 in Figs. 4(a, b)), and IDBs. Type 1b CBs are delimited by two GNB sets (GNB1 and GNB2 in Figs. 4(c, d)). Type 2 dislocation structure is formed by dislocation cells (DCs) delimited by IDBs, Figs. 5(a, b). This dislocation structure is formed in grains oriented close to [0 0 1]//TA directions where the slip type is octahedral, i.e. eight slip systems with similar Schmid factors. Type 3 dislocation structure is a complex structure formed by a homogeneous distribution of DCs and an inhomogeneous distribution of microbands (MBs) and dense dislocation walls (DDWs), Figs. 5(c - e). MBs consist of plate-type structures with a width range of 150 - 200 nm that are individually distributed along highly stressed slip planes, Fig. 5 (e). Type 3 dislocation structure is formed in grains oriented close to [1 1 1]//TA directions where slip is dominated by three slip systems on two non-coplanar slip planes. In the following, we quantitatively analyze the influence of solute hydrogen content on the dislocation structure type and boundary misorientation by combining ECCI and EBSD.

3.2.1. Type 1 dislocation structure

Combined ECCI/EBSD characterization of the dislocation structure reveals that hydrogen does not modify the morphology of the Type 1a and Type 1b cell block structures. To get a further understanding of the influence of hydrogen on the CB structure, we have quantitatively analyzed the average GNB misorientation, $\overline{\theta}_{GNB}$, of the primary GNB

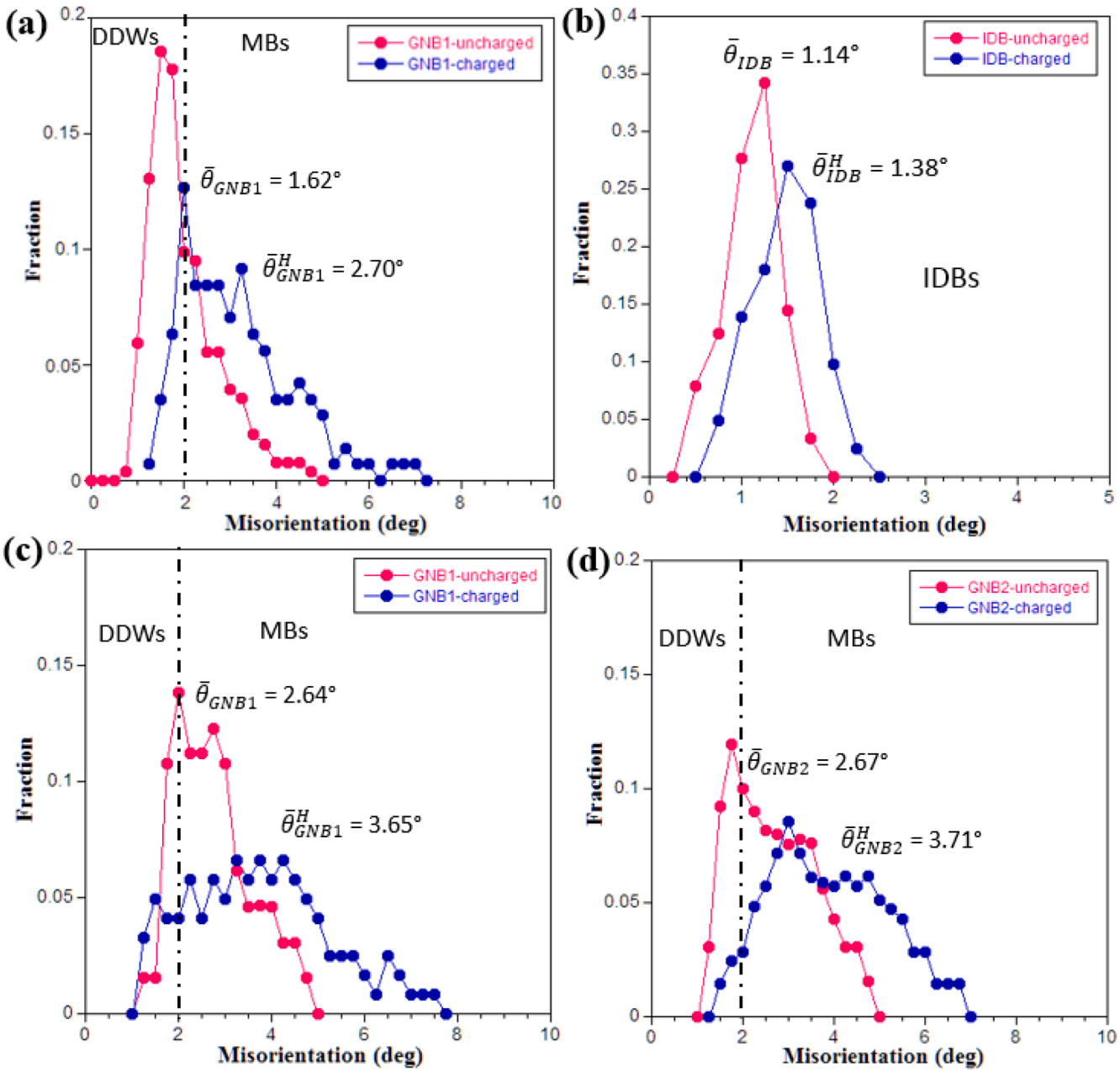

Figure 7. Quantitative analysis of the influence of hydrogen on GNB misorientation, θ_{GNB} , and IDB misorientation, θ_{IDB} , in Type 1a cell blocks (a, b) and GNB1 misorientation, θ_{GNB1} , and GNB2 misorientation, θ_{GNB2} , in Type 1b cell blocks (c, d). DDWs: Dense dislocation walls. MBs: microbands.

system in Type 1a CBs and the two GNB systems of Type 1b CBs, as well as the average IDB misorientation, $\bar{\theta}_{IDB}$, in Type 1a CBs in the uncharged and hydrogen-charged samples. GNBs and IDBs were identified on both ECC images and the corresponding grain reference orientation deviation EBSD maps (the reference point was set as the point with the lowest kernel average misorientation), as shown in Fig. 6. About 250 GNBs (30 - 50 boundaries per grain orientation) were analyzed in the uncharged and hydrogen-charged samples. 5 – 10 measurements per GNB were performed, resulting in a dataset of about 1500 GNB misorientations. About 1000 IDBs were analyzed (~200 boundaries per grain orientation). One measurement per IDB was performed in a dataset of about 1000 misorientations. The IDB misorientation was estimated from line misorientation profiles measured along the interior of the CB structure defined by GNBs.

Figs. 7(a, b) plot the influence of hydrogen on the population of GNB misorientations (a) and IDB misorientations (b) in Type 1a CBs. The influence of hydrogen on the population of GNB1 and GNB2 misorientations in the Type 1b CB structure is plotted in Figs. 7(c) and (d), respectively. GNB1 and GNB2 were identified on ECC images and EBSD maps through the boundary alignment. The plots reveal the following features. Hydrogen increases the average IDB misorientation $\bar{\theta}^{H}_{IDB}$ and average GNB misorientations $\bar{\theta}^{H}_{GNB1}$ and $\bar{\theta}^{H}_{GNB2}$ (the superscript H refers to the misorientation values in the hydrogen-charged sample). However, the effect on $\bar{\theta}^{H}_{IDB}$ is comparatively smaller than that on $\bar{\theta}^{H}_{GNB}$, as $\bar{\theta}^{H}_{IDB} - \bar{\theta}_{IDB} \sim 0.25°$ and $\bar{\theta}^{H}_{GNB}$ - $\bar{\theta}_{GNB} \sim 1°$. Interestingly, the plots reveal that the influence of hydrogen on the θ^{H}_{IDB} distribution is significantly different from that on θ^{H}_{GNB1} and θ^{H}_{GNB2} distributions. Hydrogen slightly shifts the θ^{H}_{IDB} distribution to larger misorientation values. However, it strongly modifies the θ^{H}_{GNB} distributions by increasing the population of misorientation values with $\theta^{H}_{GNB} > 2°$ and extending the θ^{H}_{GNB} distribution

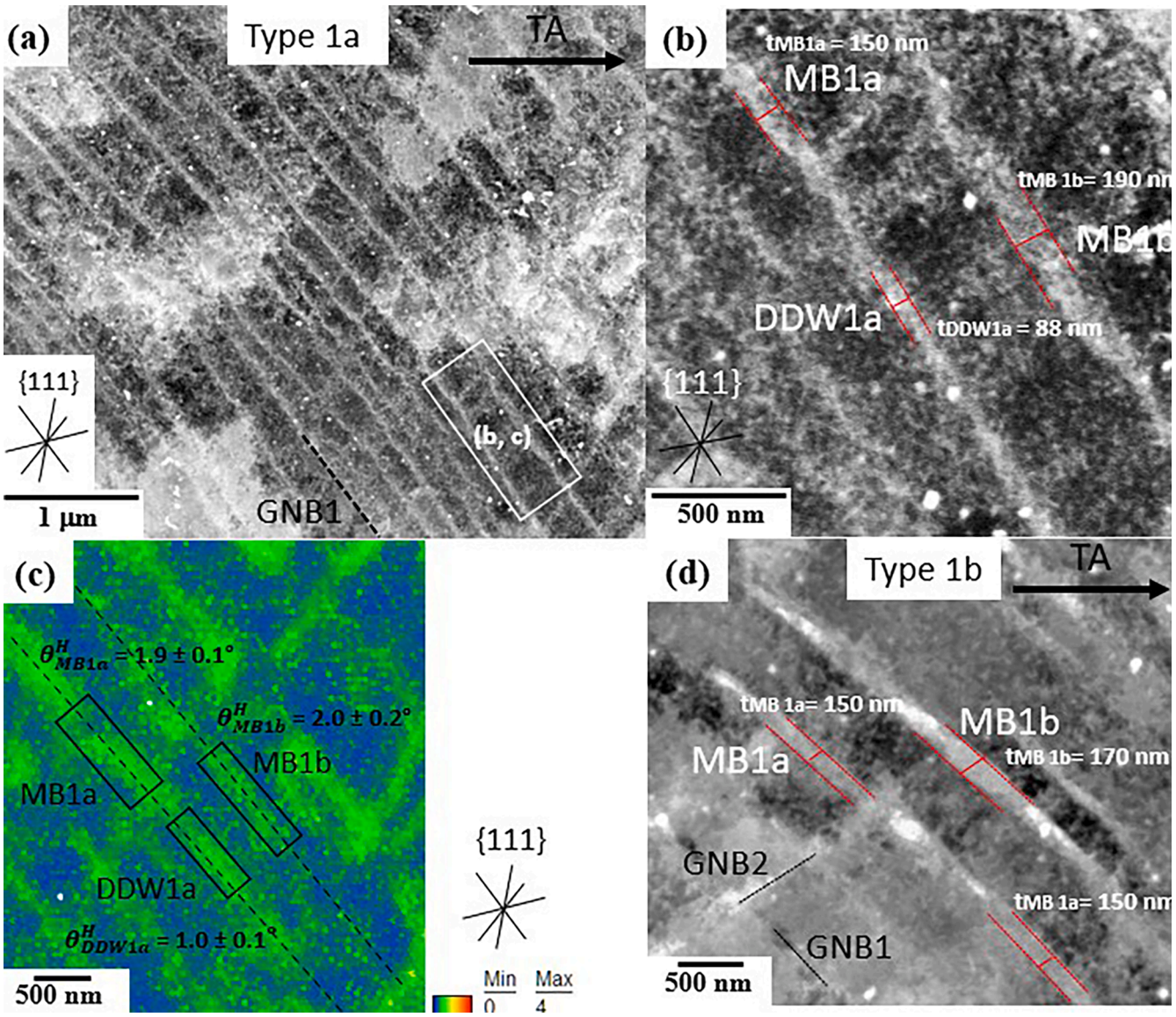

Figure 8. (a–c): Analysis of the GNB structure in a Type 1a cell block (CB) structure formed by a single GNB system (GNB1); (a, b): ECC images of the CB structure; (c): KAM-EBSD map of the CB structure shown in (b). (d): ECC image of the localized formation of microbands MB1a and MB1b along GNB1 sections in a Type 1b CB structure. DDW: Dense dislocation walls. TA: tensile axis.

to larger values (~ 7 - 8°). These results indicate that hydrogen modifies the GNB structure by promoting localized GNBs with large θ^H_{GNB}.

To gain a further understanding, the GNB structures of Type 1a and Type 1b CBs were analyzed by a combined ECCI and EBSD approach, as in [17,18]. Figs. 8(a–c) show an example of the analysis of the GNB structure in a Type 1a CB. The CB structure is formed by a single GNB system (GNB1). GNBs are formed by DDWs with an average thickness $t_{DDW} = 90 \pm 10$ nm aligned parallel to the plane trace of the primary slip system (1 -1 1). The analyzed region of the CB structure reveals the formation of two MBs (MB1a and MB1b) along localized GNB sections, Fig. 8(b). MBs are imaged as thick lenticular-shaped structures with a thickness $t_{MB} = 150 - 200$ nm and a length $l_{MB} = 1.5 - 2.0$ μm. Analysis of the boundary misorientations on the corresponding KAM-EBSD map (Fig. 8(c)) yields $\theta^H_{DDW1a} = 1.0 \pm 0.1°$, $\theta^H_{MB1a} = 1.9 \pm 0.1°$, and $\theta^H_{MB1b} = 2.0 \pm 0.2°$. These results indicate that GNB misorientations (θ_{GNB} and θ^H_{GNB}) < 2° correspond to DDWs, and GNB misorientations (θ_{GNB} and θ^H_{GNB}) > 2° are associated with MBs. Fig. 8(d) shows the localized formation of MBs (MB1a and MB1b) along GNB1 sections in a Type 1b CB structure. In this case, MBs are comparatively longer than those formed in Type 1a ($l_{MB} \sim 3 - 4$ μm). Analysis of the boundary misorientation by KAM-EBSD yields $\theta^H_{MB1a} = 5.0 \pm 0.2°$ and $\theta^H_{MB1b} = 5.6 \pm 0.2°$, which are comparatively larger than those associated with MBs formed along GNB sections in Type 1a CBs. These results suggest that MBs formed in Type 1b CBs are associated with a greater plastic accommodation. The present analysis demonstrates that the hydrogen-enhanced population of GNBs with $\theta^H_{GNB} > 2°$ is associated with the localized nucleation of MBs along GNBs, resulting in an increased $\bar{\theta}^H_{GNB}$. This finding was confirmed by BF-STEM analysis. Fig. 9(a) shows a BF-STEM image of an MB nucleated along the primary GNB system in a grain oriented close to [10 3 16]//TA direction. The BF-STEM image was taken in a "two-beam" condition using a (1 1 1)-type diffraction vector. The MB plate consists of a paired dislocation sheet structure aligned parallel to the primary GNB system (1 -1 1). Fig. 9(b) shows the corresponding diffraction pattern along the [1 0 1] zone axis. The diffraction pattern did not reveal the formation of extra diffraction spots along <2 0 0> and <2 2 0> directions, which indicates that ordered kappa-carbides were not formed in the present Fe30Mn6.5Al0.3C low-density steel [1]. This result agrees with the isothermal sections of the Fe30MnAlC system calculated by the

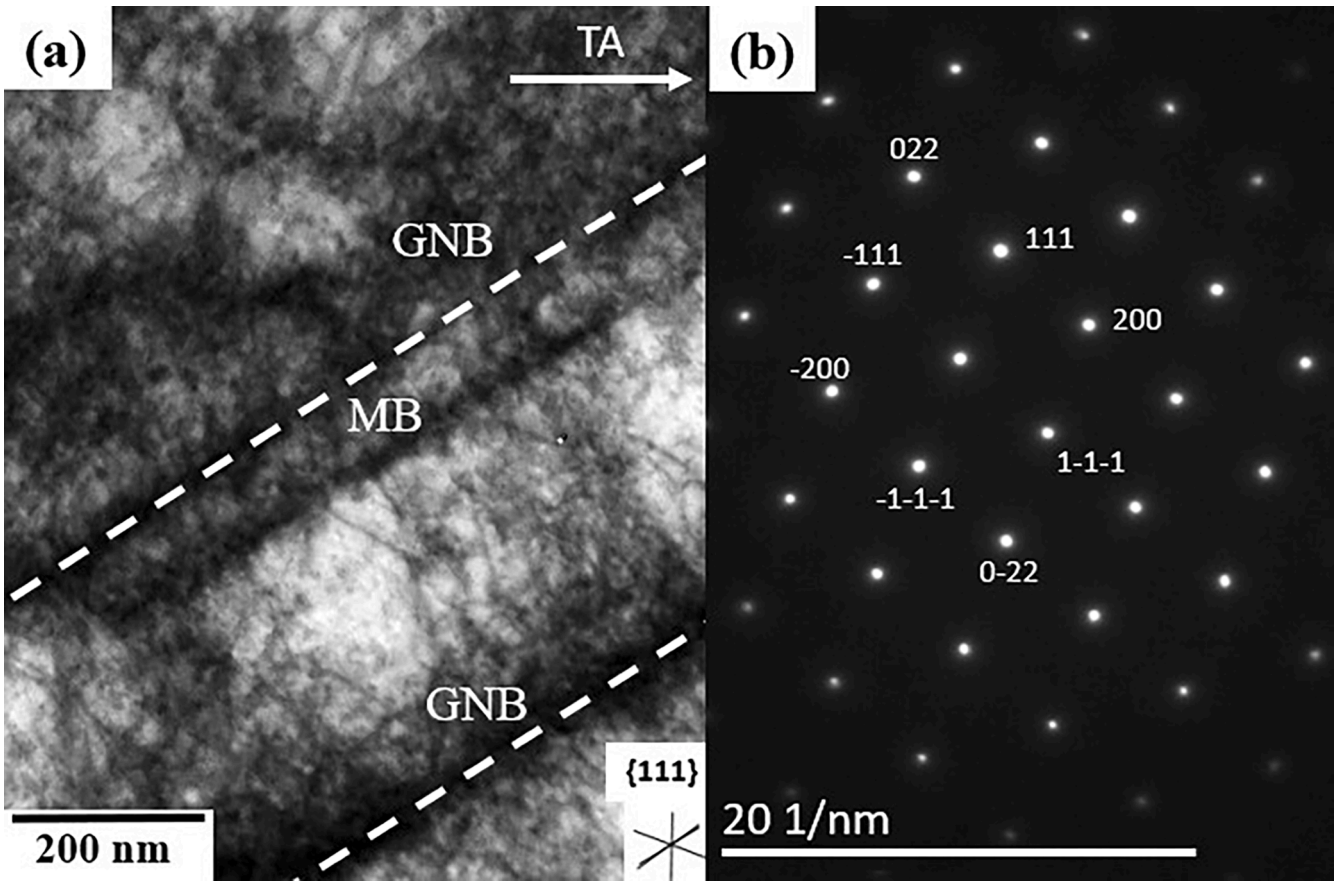

Figure 9. (a): BF-STEM image of an MB nucleated along the primary GNB system in a Type 1 CB in a grain oriented close to [10 3 16]//TA direction. The BF-STEM image was taken in a "two-beam" condition using a (1 1 1)-type diffraction vector. (b): Corresponding diffraction pattern along the [1 0 1] zone axis. GNB: Geometrically necessary boundary. MB: Microband. TA: tensile axis.

PrecHiMn-4 database [46]. The analysis demonstrates that the enhanced MB nucleation along GNBs is associated with a hydrogen-induced effect on plasticity.

3.2.2. *Type 2 dislocation structure*

ECCI analysis of the dislocation structure reveals that hydrogen strongly influences Type 2 dislocation structure through the promotion of strain localization phenomena occurring at different microstructural scales, namely, macroscopic and microscopic (Fig. 10). At the macroscale, hydrogen promotes the formation of macroscopic deformation bands (DBs) with a thickness of 10 – 30 μm that subdivide the grain, as shown in the IPF-EBSD map of Fig. 10(a). Trace analysis by EBSD confirms that DB boundaries are perpendicular to a primary slip direction, i.e. kink bands associated with inhomogeneous plasticity [47,48]. These deformation structures have been observed in the present Fe30Mn6.5Al0.3C low-density steel deformed at cryogenic temperatures [17]. On the other hand, the analysis of the interior of DBs reveals that hydrogen promotes MB formation. Figs. 10 (b–e) show the combined EBSD and ECCI analysis of the deformation structure of the interior of the deformation band DB1 oriented close to the [2 1 15]//TA direction. ECC images reveal that the deformation structure of the DB interior consists of a combination of equiaxed DCs and one crystallographic MB system corresponding to the highly stressed (1 -1 1) and (-1 1 1) slip planes. Under the current channeling conditions, MBs are imaged as bright plates with an average thickness of 150 - 200 nm that are spaced ~ 2 - 3 μm. These dislocation structures shear the interior of the deformation band DB1, resulting in a localized deformation behavior.

We have quantitatively analyzed the influence of hydrogen on the DC structure to get a further understanding of the influence of hydrogen on the Type 2 dislocation structure. At the current microscope settings and pattern analysis, the estimation of the misorientation across IDBs forming the DCs is unreliable due to the limited angular resolution of EBSD (~ 0.5° [49]). Accordingly, we only evaluated the influence of hydrogen on the average DC size, $\overline{D}_{DC}$, from ECC images on grain orientations forming the Type 2 dislocation structure. The average value was estimated as the median of the distribution. Fig. 11 plots the statistical distribution of cell sizes measured in the uncharged sample (red line) and the hydrogen-charged sample (blue line). The analysis reveals that hydrogen refines the average DC size from $\overline{D}_{DC} = 220 \pm 10$ nm (uncharged) to $\overline{D}^{H}_{DC} = 192 \pm 10$ nm (hydrogen-charged). This result agrees with former studies in fcc metals [19-22].

3.2.3. *Type 3 dislocation structure*

ECCI and BF-STEM analysis of the dislocation structure reveals that hydrogen also influences the Type 3 dislocation structure. Specifically, we find that hydrogen promotes the formation of DDWs, DBs, and MBs but has a negligible role in the DC structure. Fig. 12 shows ECC images of the dislocation structure formed in a grain oriented close to the [5 4 6]// TA direction. The ECC images were taken under (2 0 2) channeling conditions. The dislocation structure is formed by a well-developed DDW structure that is aligned close to the primary slip system (1 -1 1) [0 1 1] (Schmid factor = 0.37). Within the DDW structure, DCs with an average size $\overline{D}^{H}_{DC} = 210 \pm 10$ nm are formed. Interestingly, ECC images reveal the propagation of DBs with thicknesses ~ 0.5 – 1.0 μm and closely spaced arrays (~ 2 – 3 μm) of in-grain MB plates through localized grain regions. The average thickness of the MB plates is similar to that of the DC structure, about 200 nm. Plane trace analysis by combined EBSD and ECCI confirms that DBs and MBs are aligned close to

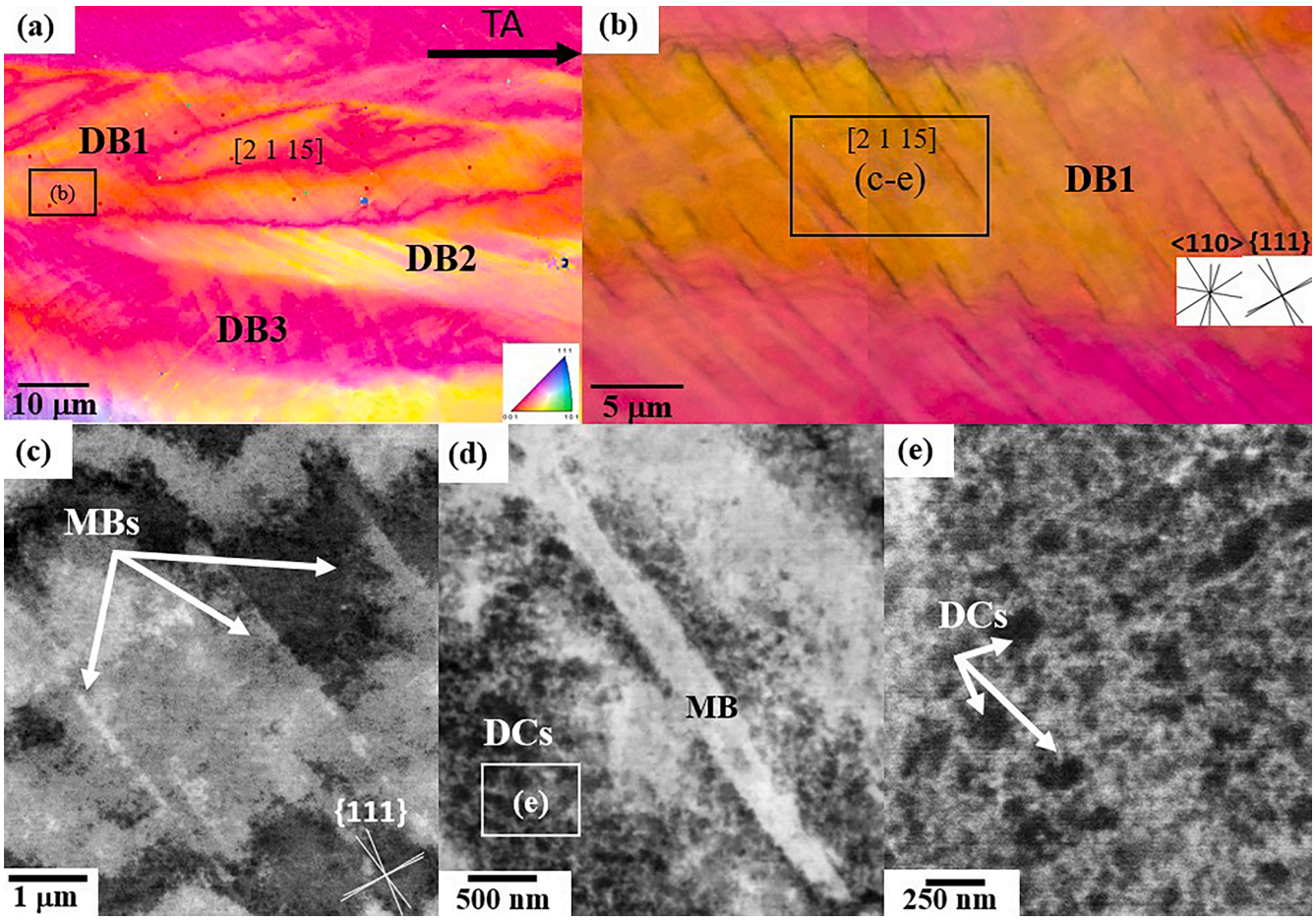

Figure 10. Influence of hydrogen on the Type 2 dislocation structure of a grain oriented close to the [1 1 18]//TA direction. (a) IPF-EBSD map showing the formation of macroscopic deformation bands (DBs). (b–e): Combined EBSD and ECCI analysis of the dislocation structure of DB1 showing microbands (MBs) and dislocation cells (DCs). TA: tensile axis.

the (-1 1 1) plane traces. This result indicates that these structures are associated with the activation of the secondary slip systems (-1 1 1) [1 0 1] (Schmid factor = 0.29) and (-1 1 1) [1 1 0] (Schmid factor = 0.24). ECC images show that the channeling contrast along the interior of DBs is not uniform, which indicates an internal orientation gradient. On the other hand, the channeling contrast observed along the MB interior is nearly uniform, which agrees with the low dislocation density observed in former studies [17].

Type 3 dislocation structures were analyzed by BF-STEM to get a further understanding of the influence of hydrogen on the dislocation-based mechanisms controlling the formation of these structures. Fig. 13 shows examples of the dislocation structure in a grain oriented close to the [6 5 8]//TA direction of the uncharged sample (a) and in a grain oriented close to the [9 7 12]//TA direction of the hydrogen-charged sample (b). BF-STEM images were taken in a "two-beam" condition using a (1 1 1)-type diffraction vector. DDWs are aligned close to the primary slip plane (1 -1 1). DBs propagating through the DDW/DC structure are visible in both grains. These structures shear DDW segments, indicated by arrows in Fig. 13. The magnitude of the shear offset produced by the DB-DDW intersections in the hydrogen-charged sample is comparatively larger. For instance, the propagation of DB2 in the uncharged sample produces a negligible shear offset of GNB segments (Fig. 13(a)). DB3 in the hydrogen-charged sample produces shear offsets of ~ 75 – 100 nm (Fig. 13(b)). DBs in these grains are associated with the activity of the secondary slip system (-1 1 1) [1 0 1]. These structures are coarser in the hydrogen-charged sample (thickness ~ 0.5 – 1.0 μm) than those formed in the uncharged sample (thickness ~ 0.3 – 0.5 μm). As shown in Fig. 13(b), individual DBs tend to merge into coarse structures in the hydrogen-charged sample. This result agrees with the slip band coarsening effect reported in austenitic steels, ascribed to hydrogen-enhanced strain localization [15,50-52].

Figs. 14, 15 show BF-STEM images of the dislocation structure in the interior of DBs formed in the region shown in Fig. 13(b). Fig. 14(a) shows the shearing of a DDW/DC structure by a DB. Fig. 14(b) shows the corresponding diffraction pattern along the [1 0 1] zone axis. Similar to Fig. 9(b), the diffraction pattern did not reveal the formation of extra diffraction spots along <2 0 0> and <2 2 0> directions. This finding indicates that the strain localization within DBs is ascribed to a hydrogen-induced effect on plasticity. STEM analysis indicates that the dislocation structure consists of a high density of long screw and mixed dislocations (~ 1 - 3 × 10^{14} m^{-2}). Examples of screw dislocations with the line direction parallel to the [1 0 1] direction are indicated by arrows in Figs. 15(a, b). Groups of closely spaced screw dislocations are commonly observed ("A" in Figs. 15(a, b)). The massive glide of secondary dislocations and their interactions with primary dislocations result in the formation of dislocation structures aligned along the secondary slip plane, such as DDWs ("B" in Fig. 15(b)) and paired screw dislocation configurations ("C" in Fig. 15(b)). Interestingly, dissolved DDW segments are visible ("D" in Figs. 15(a, b)). This effect is associated with the trapping of screw dislocations by DDWs, which makes them mechanically unstable [53]. Besides these configurations, the interaction between (1 -1 1) [0 1 1] primary dislocations and (1 -1 -1) [-1 0 -1] secondary dislocations promotes the formation of [-1 1 0] sessile Lomer-Cottrell dislocations [54]. The screw and mixed dislocations exhibit numerous small cusps associated with jogs ("J" in Fig. 15(c)). These cusps play a key role in the dislocation multiplication process as

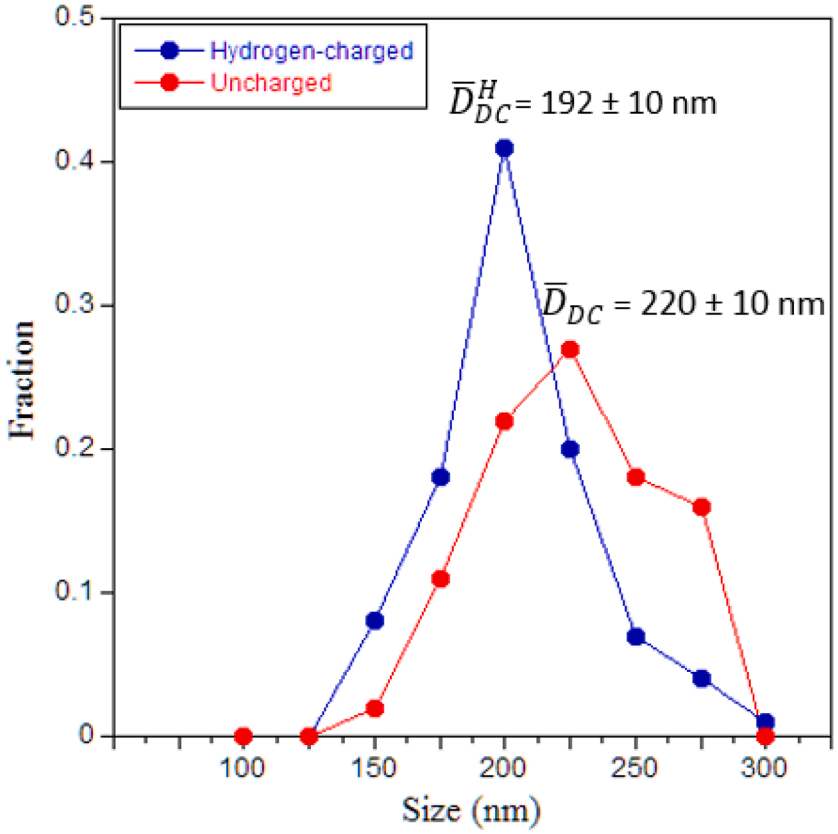

Figure 11. Effect of hydrogen on the distribution of the dislocation cell size (D_{DC}) in type 2 dislocation structures. D_{DC} was estimated from ECC images.

they act as pinning points for single-ended sources of dislocations. Analysis of the alignment of the dislocation lines reveals cross-slipping and double-cross slipping dislocations ("CS" in Figs. 15(c, d)). As an example, the analysis of a double-cross slipped dislocation is shown in Fig. 15(d). The (-1 1 1) [1 0 1] screw dislocation cross-slips onto the (-1 -1 1) plane and then cross-slips back onto another (-1 1 1) plane. These observations indicate that dislocation cross-slip is activated within DBs, enabling the propagation of screw dislocation through the DDW/DC structure.

Fig. 16 shows the effect of hydrogen on the cell boundary misorientation (θ_{DC}) distribution (a) and the cell size (D_{DC}) distribution (b). D_{DC} was estimated from ECC images and θ_{DC} was measured from KAM-EBSD maps where cell boundaries were identified by combined ECCI and EBSD. Cell boundaries with $\theta_{DC} < 0.5°$ are not considered due to the limited angular resolution of the EBSD approach used in this study (~ 0.5°). We find that hydrogen refines the average DC size from $\overline{D}_{DC} = 236 \pm 10$ nm (uncharged) to $\overline{D}^{H}_{DC} = 212 \pm 10$ nm (hydrogen-charged). This result is in line with the measured influence of hydrogen on the Type 2 dislocation structure. However, our EBSD data indicates that hydrogen plays a small effect on $\overline{\theta}^{H}_{DC}$, as both misorientation populations are similar with $\overline{\theta}_{DC} = 0.87° \pm 0.05°$ (uncharged sample) and $\overline{\theta}^{H}_{DC} = 0.90° \pm 0.05°$ (hydrogen-charged sample).

3.3. Fractography

Fig. 17 shows typical fracture surfaces of the Fe30Mn6.5Al0.3C low-density steel in the uncharged state (a - c) and hydrogen-charged state (d - f). Both samples exhibit a fully ductile fracture characterized by the growth and coalescence of microvoids. This observation indicates that hydrogen does not significantly modify the fracture behavior of the present FeMnAlC low-density steel. The analysis of the fracture surfaces reveals that the size distribution of the dimples in the uncharged sample is heterogeneous, with areas containing small-sized dimples (2 – 3 μm), Fig. 17(b), and regions containing large-sized dimples (4 - 8 μm), Fig. 17 (c). Comparatively, the dimple size distribution in the hydrogen-charged sample is finer (Figs. 17(e, f)), namely, it is in the size range of 1.5 to 3.0 μm. This effect is associated with void sheets, i.e. aggregation of small voids due to the increased number of void nucleation events produced by hydrogen-enhanced strain localization phenomena [55-57]. The micron size of the dimples observed in the fracture surfaces is related to the large grain size (~ 150 μm). This finding is similar to that reported in hydrogen-charged samples of austenitic stainless steels 316L and HP160 tested at similar conditions to those used in the present work [55].

4. Discussion

4.1. Influence of hydrogen on the mechanical behavior

The present study shows that at the current deformation conditions (initial strain rate of 5.0×10^{-5} s^{-1} in laboratory air at 295 K), a hydrogen content of 101 mass ppm increases the yield stress, flow stress, and ductility of the present Fe30Mn6.5Al0.3C low-density steel. Solid-solution hardening by hydrogen has been reported in austenitic stainless steels [14,58,59], Ni-based alloys [60-62], and fcc high-entropy alloys [63]. The hardening effect strongly depends on the hydrogen content, material, and testing conditions and may lead to an increase in the yield stress of up to a few hundred MPa. Comparatively, the strengthening associated with solute hydrogen observed in the present steel (27 MPa) is smaller than that typically observed in austenitic stainless steels. For instance, in our recent study [64], we obtained a hydrogen-induced increase of the yield stress of ~ 60 MPa in a 310S stainless steel hydrogen-charged and tested at similar conditions to those used in this study. Interestingly, the influence of hydrogen on ductility observed in this study is unusual, as hydrogen commonly

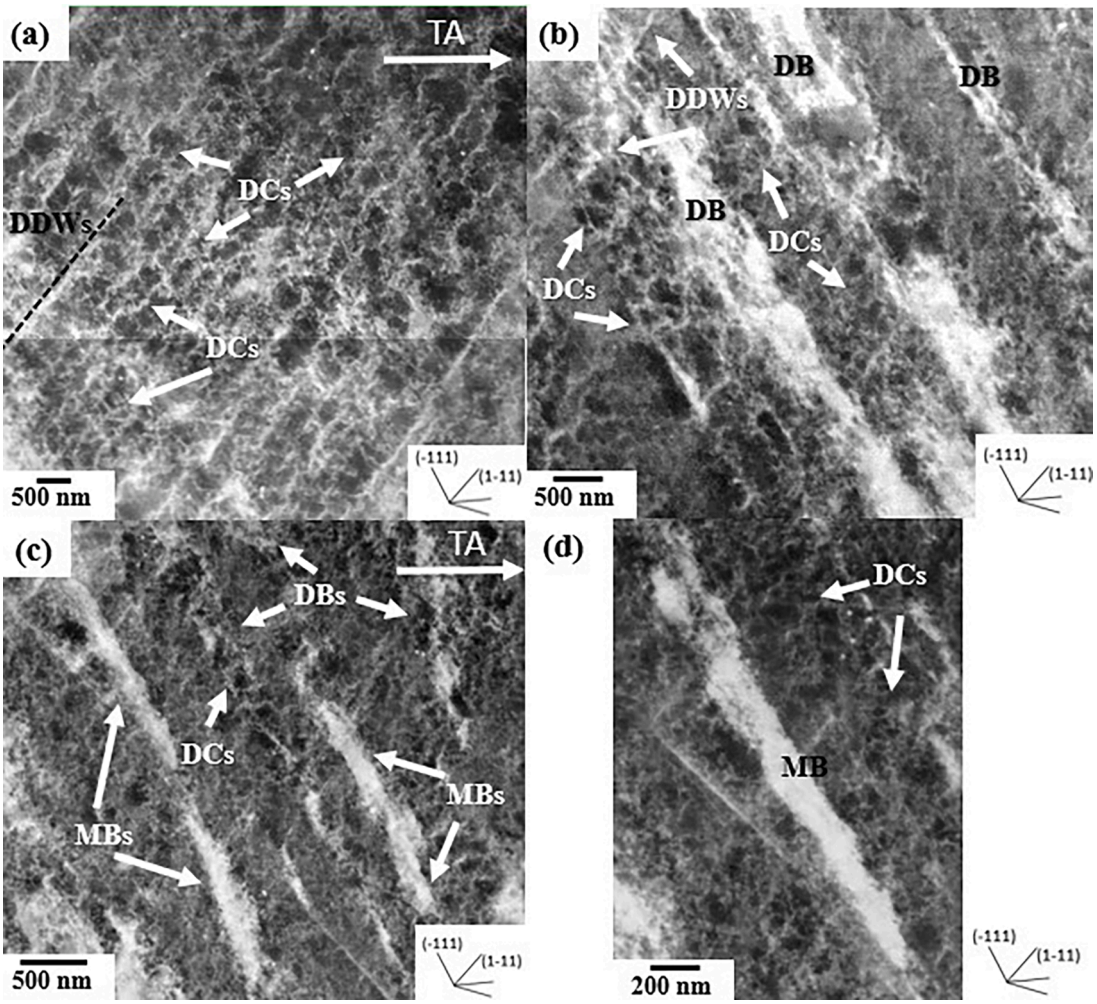

Figure 12. Influence of hydrogen on the Type 3 dislocation structure of grains oriented close to the [5 4 6]//TA direction. (a): ECC image of the dislocation structure consisting of dense dislocation walls (DDWs) and dislocation cells (DCs). (b): ECC image of an area containing DBs propagating through the DDW/DC structure. (c): ECC image of an area containing DBs and microbands (MBs) propagating through the DDW/DC structure. (d): Detail of an MB imaged as a bright plate under the current (2 0 2) channeling conditions. TA: tensile axis.

promotes the degradation of the ductility in fcc alloys (hydrogen embrittlement) owing to the premature failure accompanying intergranular or cleavage-like fracture features [15,22,52,61-63]. The influence of the deformation structure on the HE resistance is analyzed in Section 4.3.

4.2. *Influence of hydrogen on the dislocation structure*

Our former work has shown that the room-temperature deformation structure of the austenitic Fe30Mn6.5Al0.3C low-density steel mainly consists of dislocation structures associated with homogeneous plasticity, such as DCs, DDWs, and CBs [18]. The present study shows that at the current deformation conditions (295 K and initial strain rate of 5.0×10^{-4} s^{-1}), hydrogen has a small influence on DCs (cell size refinement of ~ 10%) while enhancing the formation of DDWs. These findings suggest that hydrogen has a greater influence on GNBs than on IDBs, which agrees with former studies in fcc metals [19,21,23]. The hydrogen-induced stabilization of GNBs has been attributed to the hydrogen-induced shielding of the dislocation elastic field, leading to a reduced Peach-Kohler force and, hence, the stabilization of primary dislocation configurations with reduced dislocation spacing. The dislocation cell size refinement reported in hydrogen-charged fcc metals has been ascribed to dislocation trapping by incidental boundaries due to Cottrell atmospheres of hydrogen [19]. In Ni and a Ni16Cr alloy, a hydrogen-induced cell size refinement of ~ 25 - 75 % was reported at similar deformation conditions to those used in the present study [19-22]. The small influence of solute hydrogen in the DC structure of the present steel suggests that dislocation trapping by incidental boundaries induced by hydrogen is limited in the present steel. Interestingly, hydrogen significantly enhances the formation of dislocation structures associated with inhomogeneous plasticity (DBs) and strain localization (MBs). We refer to these effects as hydrogen-enhanced deformation banding (HEDB) and hydrogen-enhanced microbanding (HEMB), respectively. SAD analysis (Figs. 9, 14) confirms that these deformation mechanisms are ascribed to hydrogen-induced effects on plasticity. In the following sections, we analyze the dislocation-based processes controlling the hydrogen-induced formation of DBs and MBs.

4.2.1. *Hydrogen-enhanced deformation banding (HEDB)*

ECC and BF-STEM observations show that HEDB is associated with the formation of two types of DBs, namely, macroscopic (thickness of 10 – 30 μm) kink-bands in grains oriented close to <0 0 1>//TA directions (Figs. 10(a, b)) and submicron DBs in grains oriented close to <1 1 1>// TA directions (Figs. 12 - 14). These DBs are associated with two different types of inhomogeneous plasticity. The formation of kink bands in fcc metals is commonly associated with localized lattice sliding and lattice rotations induced by macroscopic constraints imposed on the specimen geometry [48] and strain localization assisted by slip band intersections

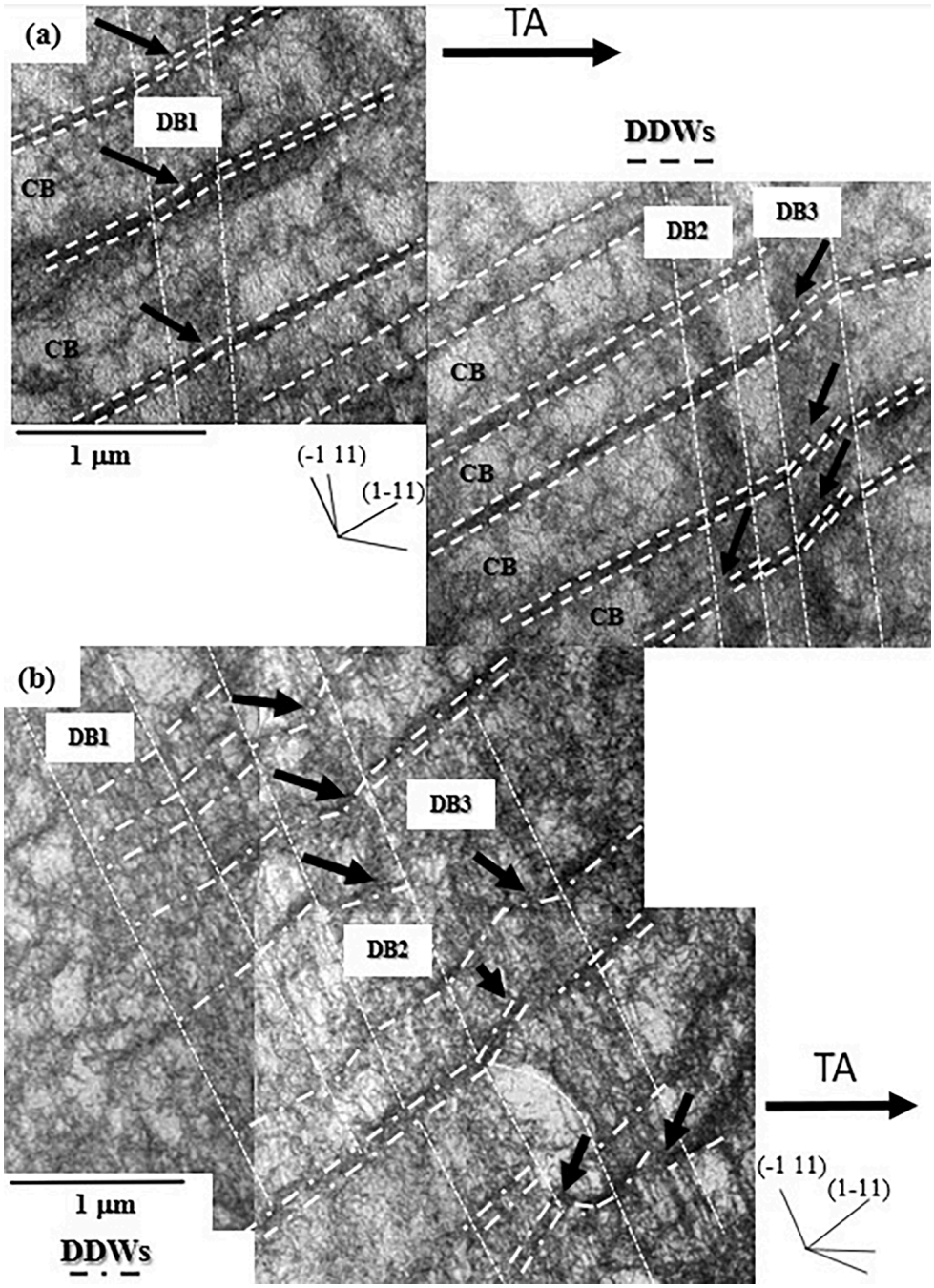

Figure 13. BF-STEM images of the dislocation structure showing deformation bands (DBs) in a grain oriented close to the [6 5 8]//TA direction of the uncharged sample (a) and in a grain oriented close to the [9 7 12]//TA direction of the hydrogen-charged sample (b). BF-STEM images were taken in a "two-beam" condition using a (1 1 1)-type diffraction vector. DDWs: Dense dislocation walls. TA: tensile axis.

[65,66]. Kink bands are aligned parallel to the trace of the slip system associated with the stronger strain field, which is determined by the grain orientation and constraints imposed by neighboring grains [66]. The formation of kink bands in the hydrogen-charged sample suggests that the generation of lattice rotations by slip band intersections is enhanced by hydrogen. Although the details are still unclear, this effect is likely associated with the large strain field of hydrogen-induced slip bands, as reported in austenitic steels [51,52,67].

BF-STEM images (Fig. 15) reveal a high plastic activity in the interior of submicron DBs formed in the grain oriented close to <1 1 1>//TA directions of the hydrogen-charged sample. The intense plastic activity is associated with the glide of secondary dislocations (dislocation density $\sim 1 - 3 \times 10^{14}$ m^{-2}), resulting in the localization of plasticity. Fig. 13 shows that DBs were formed in grains oriented close to <111>//TA directions of both samples, namely, uncharged and hydrogen-charged, which indicates that the intense plastic activity observed in the hydrogen-induced DBs is not associated with the deformation constraints but with the influence of hydrogen on plasticity. Hydrogen-enhanced strain localization has been reported in several austenitic steels, resulting in the coarsening of slip bands [13-15]. Although the details of the underlying dislocation-based mechanisms are still unclear, this effect has been ascribed to the locking of dislocations by hydrogen atmospheres [15] and the hydrogen-induced reduction of dislocation cross-slip [25,26]. Interestingly, former studies have revealed that solute hydrogen enhances the dislocation mobility in austenitic steels due to the elastic shielding of the strain field associated with dislocations [25,

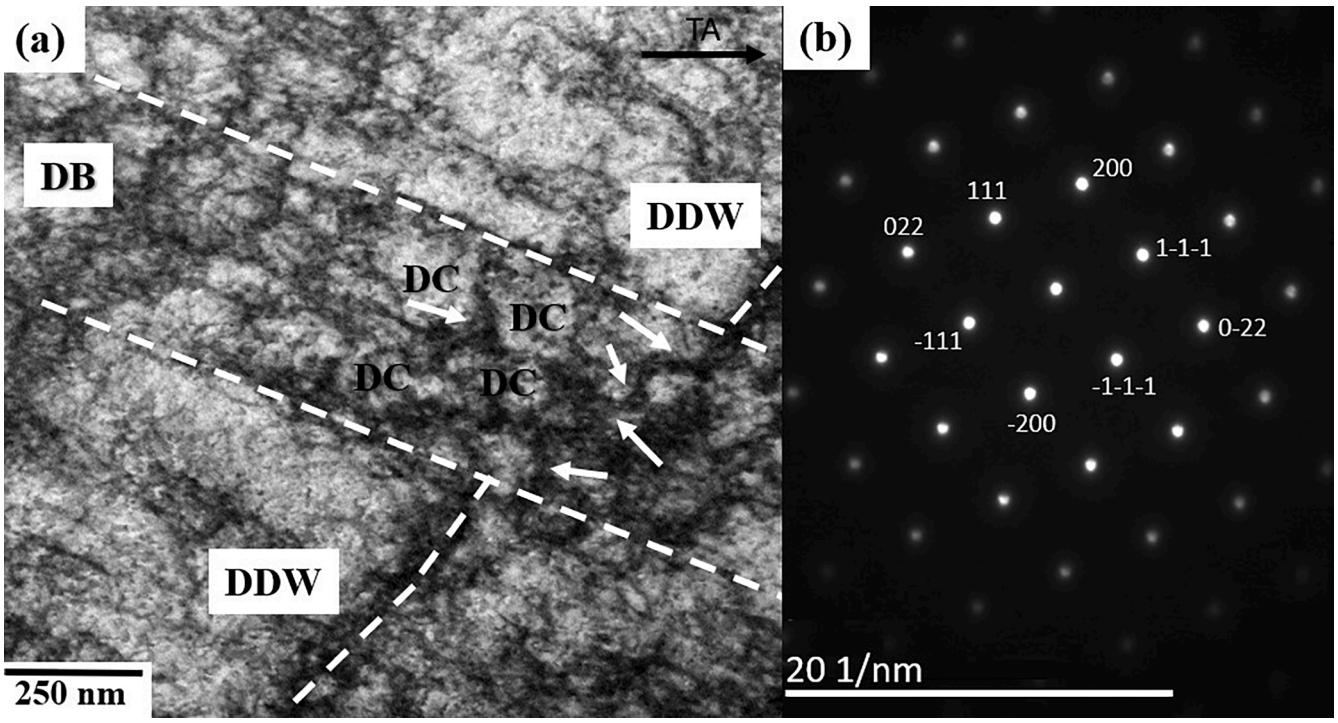

Figure 14. (a) BF-STEM image showing the shearing of a DDW/DC structure by a DB in a grain oriented close to the [9 7 12]//TA direction of the hydrogen-charged sample. Sheared DC walls are indicated by arrows. BF-STEM image was taken in a "two-beam" condition using a (1 1 1)-type diffraction vector. (b): Corresponding diffraction pattern along the [1 0 1] zone axis. TA: tensile axis.

26]. In particular, Ogawa et al. [64] have shown that at the current deformation conditions (295 K and initial strain rate of 5.0×10^{-5} s^{-1}), the hydrogen-dislocation interaction results in solute drag in an austenitic FeCrNi steel. This effect tends to promote the intermittent mobility of dislocations that favor the massive glide of dislocations, such as that observed in the interior of DBs (Fig. 15). Further work is needed to clarify the influence of hydrogen content and deformation conditions on the hydrogen-induced plasticity effects that control HEDB.

4.2.2. Hydrogen-enhanced microbanding (HEMB)

ECC and BF-STEM observations of the hydrogen-induced dislocation structure (Figs. 8, 9, 10, and 12) show that HEMB is associated with hydrogen-induced shear localization generated in two distinguishable microstructural locations, namely GNB structure of CBs and localized regions of the grain interior associated with DBs. The underlying hydrogen-induced mechanisms associated with HEMB are depicted in Fig. 18. Figs. 8, 9 show the hydrogen-induced formation of MBs along the pre-existing GNB structure of Type 1a and Type 1b CBs. This effect can be explained by the boundary-splitting model introduced by Hughes [68,69]. We refer to this mechanism as GNB-assisted MB nucleation (Fig. 18(a)). In this model, GNBs assist the MB formation through their splitting, resulting in the nucleation of localized MBs along the GNB structure. The driving force for MB nucleation is the increased misorientation across GNBs upon deformation. As the analysis of GNB misorientations indicates (Fig. 7), GNB-assisted MB nucleation is activated in both samples, namely, uncharged and hydrogen-charged. Interestingly, EBSD analysis reveals that GNB-assisted MBs formed in the hydrogen-charged sample are associated with comparatively larger lattice rotations ($\theta^{H}_{MB} \sim 2$ - 8°) than their counterparts formed in the uncharged sample ($\theta^{H}_{MB} \sim 2$ - 3°). This result indicates that GNB splitting is promoted by the enhanced storage of geometrically necessary dislocations (GNDs) associated with localized shear induced by hydrogen, resulting in a local increase in the GNB misorientation. Although the dislocation-based process controlling this effect is still unclear, it can be ascribed to the hydrogen-induced stabilization of dislocation pile-ups with reduced dislocation spacing during the early stages of deformation, as suggested by Girardin et al. [19]. These dislocation configurations evolve with the activation of secondary slip into GNB-type structures such as DDWs with a reduced dislocation spacing and, hence, higher boundary misorientation. This process can be eventually promoted by hydrogen trapping by the elastic stress field of edge dislocations forming the DDWs [23,70-72]. The localized nature of the GNB splitting process suggests that the hydrogen-enhanced boundary misorientation effect is not uniform along the GNB structure.

In-grain microbanding has been ascribed to the evolution of mechanically unstable primary dislocation configurations into a more mechanically stable dislocation configuration due to massive secondary slip activation. According to Jackson's model [73,74], this process can be ascribed to the avalanche glide of massive cross-slipped groups of dislocations on latent slip planes that shear the primary dislocation configurations, resulting in closely spaced dislocation sheets. Further dislocation reactions involving dislocation annihilation and Lomer-Cottrell lock formation contribute to the mechanical stabilization of MBs [75,76]. BF-STEM analysis of the dislocation configuration of DBs in the hydrogen-charged sample (Fig. 15) reveals the occurrence of the main dislocation-related features that promote HEMB in the grain interior. These are massive glide of groups of secondary dislocations that shear the existing CB/DC structure resulting in the formation of closely-spaced dislocation sheets of thickness close to the DC size and the cross-slipping and double-cross slipping of screw dislocations that enable dislocation annihilation and, hence, the plastic relaxation of the dislocation sheets that evolve into MBs. Besides these features, analysis of the activated slip systems indicates the potential formation of Lomer-Cottrell locks that contribute to the mechanical stabilization of MBs. This analysis suggests that MBs are formed within DBs, which agrees with ECC images of regions containing DBs and MBs (Fig. 12). We refer to this mechanism as DB-assisted MB nucleation, Fig. 18 (b).

In this context, it is worth commenting on the activity of dislocation cross-slip within DBs formed in the hydrogen-charged sample. This dislocation behavior is unexpected according to the hydrogen-induced

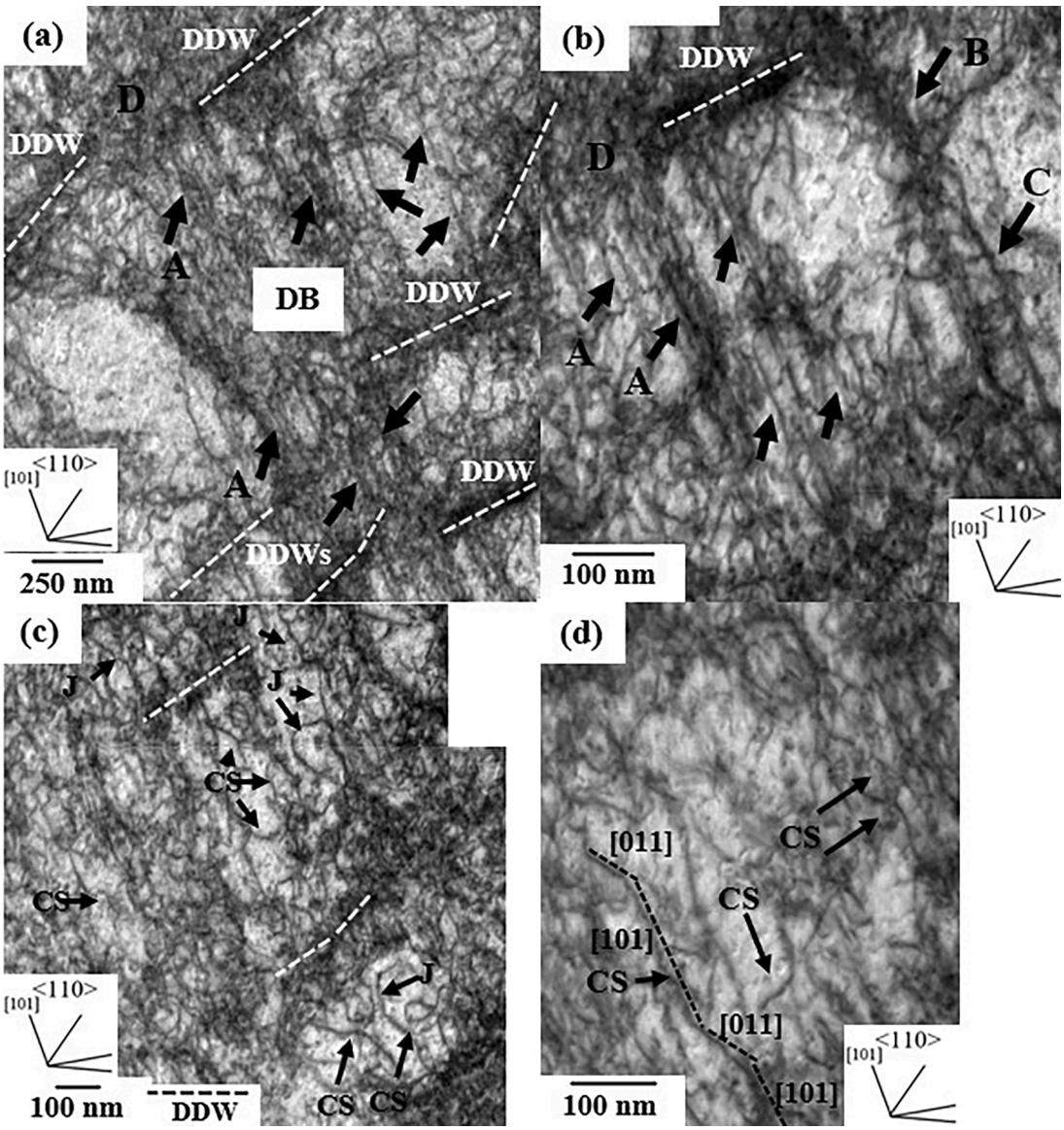

Figure 15. BF-STEM images of the dislocation structure in the interior of DBs formed in the hydrogen-charged sample are shown in Fig. 13(b). BF-STEM images were taken in a "two-beam" condition using a (1 1 1)-type diffraction vector. A: Groups of closely spaced screw dislocations. B: Dense dislocation wall (DDW); C: Paired screw dislocation configuration; D: Dissolved DDW segments; CS: Cross-slipped and double-cross slipped dislocations.

reduction of cross-slip predicted in fcc metals by atomistic calculations [15,26,29]. As discussed above, hydrogen-induced reduction of dislocation cross-slip has been invoked to explain hydrogen-induced strain localization in austenitic steels [25,26]. The present observations suggest that solute hydrogen does not fully disable cross-slip of screw dislocations within DBs, which enables microbanding [73,74]. If we calculate the stress required to expand a screw segment of length L onto the cross-slip plane, $\tau_{critical} = 1.5\ Gb/L$ [54], where G is the shear modulus and b is the dislocation Burgers vector, it yields $\tau_{critical} \sim 350$ - 520 MPa for $L = 50$ - 75 nm (estimated from BF-STEM images of cross-slipped dislocations). The calculated stress range is higher than the resolved shear stress estimated from the applied load, $\tau \sim 330$ MPa. This analysis indicates that the internal stress field of DBs, mainly associated with the long-range stress field of the internal dislocation configuration, promotes dislocation cross-slip. Internal stresses can promote cross-slip by supplying work for constricting partial separations on the primary plane and expanding the dislocation segment on the cross-slip plane. This effect has been recently predicted in slip bands of fcc metals by three-dimensional dislocation dynamics [77]. Further work is needed to clarify the influence of hydrogen content on the dislocation-cross slip activity in austenitic FeMnAlC low-density steels and its effect on dislocation plasticity.

4.3. The effect of HEMB on HE resistance

The key finding of the present study is the high HE resistance exhibited by the Fe30Mn6.5Al0.3C low-density steel at the current deformation conditions (295 K and initial strain rate of 5.0×10^{-5} s^{-1}). The analysis of the fracture surfaces of the uncharged and hydrogen-charged samples indicates that hydrogen does not modify the ductile fracture behavior of the steel. We find that hydrogen refines the dimple size. This effect is associated with void sheets produced by hydrogen-enhanced strain localization phenomena [15,16], which agrees with the characterization of the hydrogen-induced deformation structure. The ductile fracture behavior of the hydrogen-charged sample suggests that the potential transportation of hydrogen by mobile dislocations [78, 79] does not promote grain boundary cracking. This analysis suggests that hydrogen-induced effects on the dislocation structure can play an

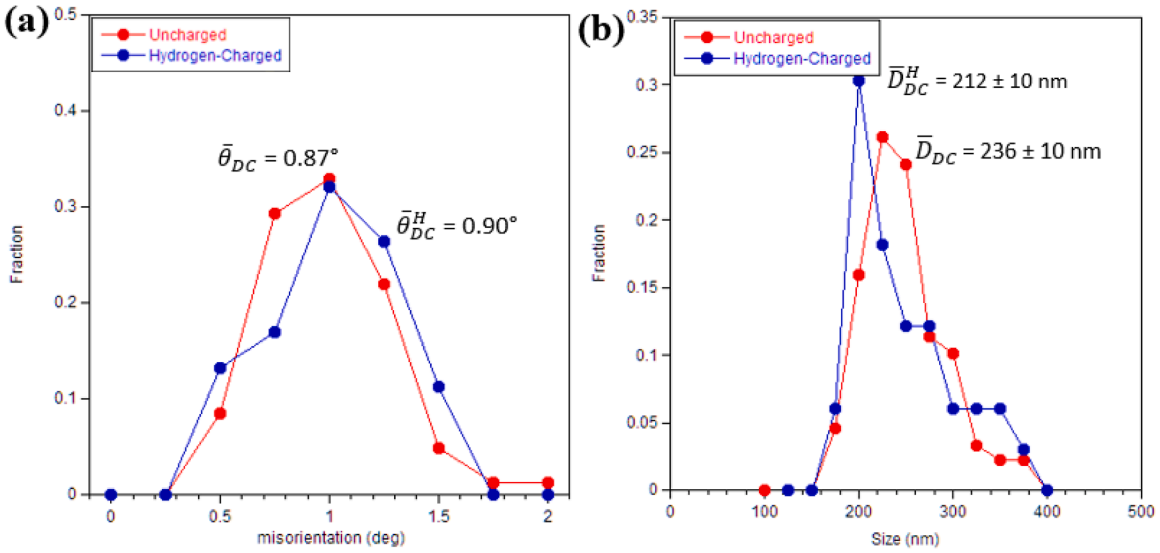

Figure 16. Effect of hydrogen on the distributions of the cell boundary misorientation, θ_{DC} , (a) and cell size, D_{DC}, (b) in type 3 dislocation structures. D_{DC} was estimated on ECC images. θ_{DC} was obtained from EBSD data.

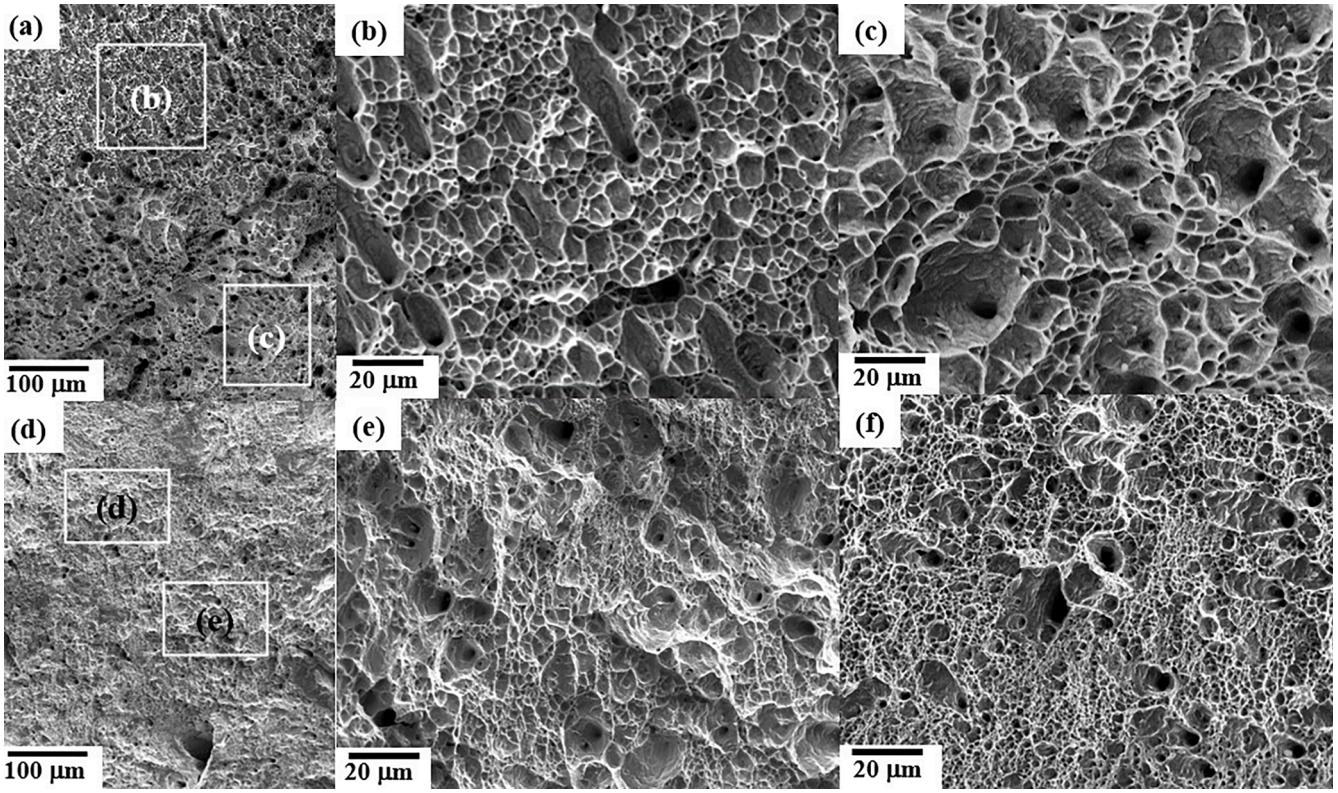

Figure 17. SEM fractographs of the uncharged (a-c) and the hydrogen-charged (d-f) tensile samples. (b, c) and (e, f) correspond to magnified images taken from the rectangular frames marked in (a) and (d), respectively.

active role in the high HE resistance exhibited by the steel. The main characteristic of the hydrogen-induced deformation structure is the occurrence of the HEDB and HEMB effects. HEDB is ascribed to hydrogen-enhanced inhomogeneous deformation behavior due to specific hydrogen-induced effects on plasticity (section 4.2.1). From a plasticity standpoint, HEDB is a deformation mechanism that accommodates the macroscopic and submicron hydrogen-induced inhomogeneous strain gradients. These structures can potentially activate GB damage mechanisms via DB-assisted void formation and coalescence along grain boundaries [16]. Our observations reveal that the interaction of submicron DBs with the existing primary DDW/DC structure leads to the localized formation of MBs in the hydrogen-charged sample via the DB-assisted MB nucleation mechanism (Fig. 18(b)). This deformation mechanism accommodates localized shear deformation by storing GNDs along MB boundaries [17,80]. Interestingly, our analysis in Section 4.2 has revealed a key effect of HEMB on plasticity, namely, the relaxation of the internal stress field of DBs. As the fracture surfaces of the uncharged and hydrogen-charged samples show (Fig. 17), this

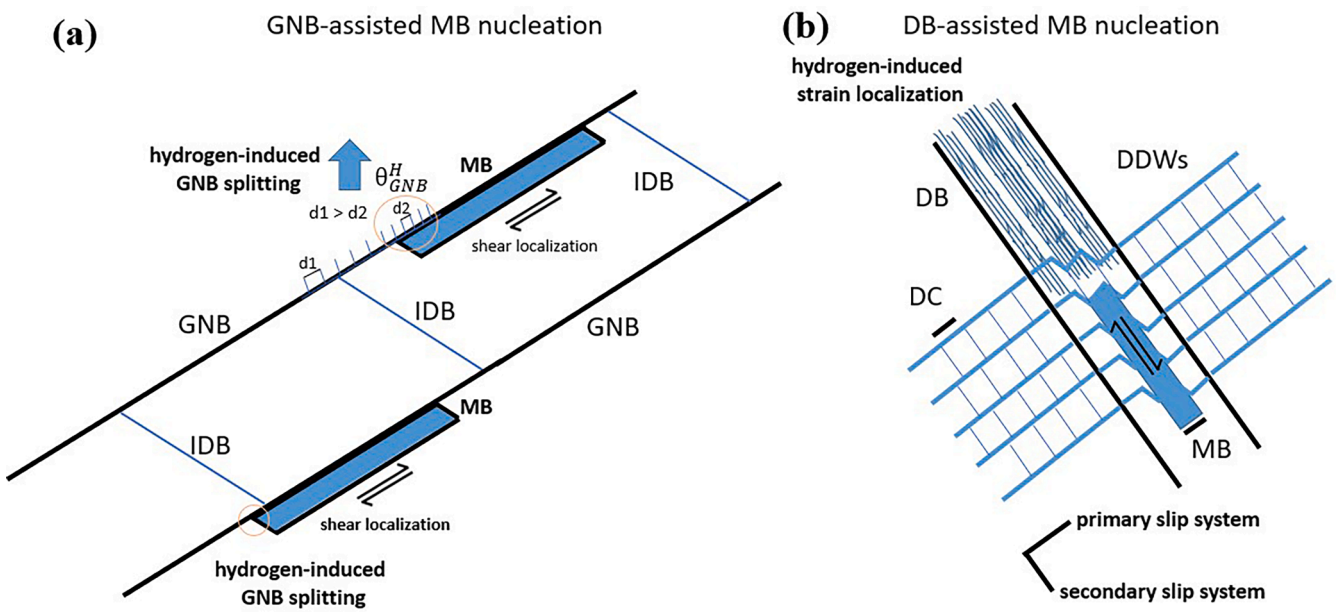

Figure 18. Schematic of the hydrogen-induced microband (MB) nucleation mechanisms. (a): GNB-assisted MB nucleation. (b): DB-assisted MB nucleation.

effect is key to preventing the activation of GB damage mechanisms associated with hydrogen-induced strain localization phenomena, such as grain boundary cracking via slip band-assisted void formation and coalescence along grain boundaries reported in austenitic steels [13-16].

These findings indicate that HEMB plays a relevant role in the deformation behavior of strain localization gradients associated with DBs by promoting the plastic accommodation within them and mitigating the activation of damage mechanisms. These effects contribute to the strain-hardening capacity and, hence, the HE resistance of the steel. The strain level required to form the dislocation structures that assist in the hydrogen-induced MB nucleation mechanisms ($\varepsilon \sim 0.1 - 0.3$) indicates that HEMB can be a relevant deformation mechanism in moderated-high ductile fcc alloys when exposed to hydrogen. It is worth stressing that although the influence of hydrogen content on HEMB is unknown, the present study suggests that a critical hydrogen content trapped in the dislocation structure of GNBs, slip bands, and DBs is needed to promote HEMB with a sufficient frequency to play a relevant role in the material's plasticity. Further work is required to evaluate the influence of hydrogen content on HEMB and its contribution to the mechanical behavior of austenitic FeMnAlC low-density steels.

4.4. Comparative analysis of the HE resistance of austenitic steels

In this section, we compare the HE resistance level exhibited by the present Fe30Mn6.5Al0.3C low-density steel to that reported in austenitic steels and multicomponent fcc alloys with a range of tensile mechanical properties similar to those of the present steel. We have only analyzed materials charged under gaseous hydrogen conditions at high pressure (~10 – 100 MPa) where hydrogen content is macroscopically constant within the sample to avoid the effect of surface hydrogen gradient on the deformation structure and fracture behavior. Only studies that analyze the fracture behavior are considered. Fig. 19 plots the values of the HE susceptibility index (IHE) against the ultimate tensile strength, UTS, of selected austenitic steels and fcc high-entropy and medium-entropy alloys (HEA and MEA). IHE is defined as IHE $= 1 - \varepsilon_f^H/\varepsilon_f$, where ε_f^H is the elongation to fracture of the material exposed to hydrogen and ε_f is that of the uncharged material [81]. The data are summarized in Table 2. The plot of Fig. 19 is divided into three areas according to the level of HE resistance: low (IHE > 0.1), moderated (0.1 > IHE > 0), and high (IHE < 0). Austenitic steels with low HE resistance are characterized by the activation of brittle fracture modes, such as intergranular (IG), transgranular (TG), and quasi-cleavage (QC). These fracture mechanisms are associated with the massive activation of deformation twinning (FeMnC TWIP steels [82,83]) and the promotion of intense slip localization (Fe16Cr10Ni (316) and Fe18Cr8Ni (304) steels [55]). Austenitic steels with moderated/high HE resistance, such as 17.5Cr12Ni (316L) steel [55,84], 20.7Cr9.7Ni4Mn2Mo (HP160) steel [55], and 18Cr12.5Ni (317L) steel [83], are characterized by a small influence of hydrogen on the fracture behavior. These materials exhibit either ductile fracture or a combination of ductile fracture and IG fracture. Recent calculations on the influence of hydrogen content in the critical stress intensities for brittle cleavage (K_{Ic}) and dislocation emission (K_{Ie}) have shown that the high HE resistance of 316L steel can be ascribed to the influence of hydrogen on the fracture-free energy and unstable stacking fault energy that makes the ratio $K_{Ic}/K_{Ie} > 1$ even at high hydrogen content (~100 mass ppm) [85]. High HE-resistant fcc alloys, such as 25Fe25Ni25Cr25Co [86], CoCrFeMnNi [34], 33Co33Ni33V [32], and 310S steel [87], are characterized by a combination of ductile and IG fracture. The high HE resistance of these alloys is associated with the hydrogen-induced activation of nanotwinning (hydrogen-enhanced densified twinning, HEDT, effect), resulting in enhanced strain-hardening capacity. Fig. 19 shows that the present Fe30Mn6.5Al0.3C low-density steel with a hydrogen content of 101 mass ppm exhibits a HE resistance comparable to that of high HE-resistant alloys containing a hydrogen content of 75 – 130 mass ppm, which confirms the high HE resistance of the present steel. This finding indicates that hydrogen-induced effects on plasticity, such as HEDT and HEMB, can play an active role in the HE resistance of fcc alloys by promoting the material's capacity to accommodate plasticity when exposed to hydrogen. The accommodated strain level, hardening, and damage associated with these effects dictate the mechanical behavior. In particular, the capacity of HEMB to mitigate damage associated with hydrogen-induced strain localization phenomena needs to be explored in other fcc alloys to implement this effect in design approaches to HE-resistant austenitic fcc alloys.

5. Conclusions

The influence of 101 mass ppm hydrogen content on the dislocation structure and deformation behavior of an austenitic Fe30Mn6.5Al0.3C (wt.%) low-density steel was evaluated on the main deformation texture components by several electron microscopy techniques, such as electron

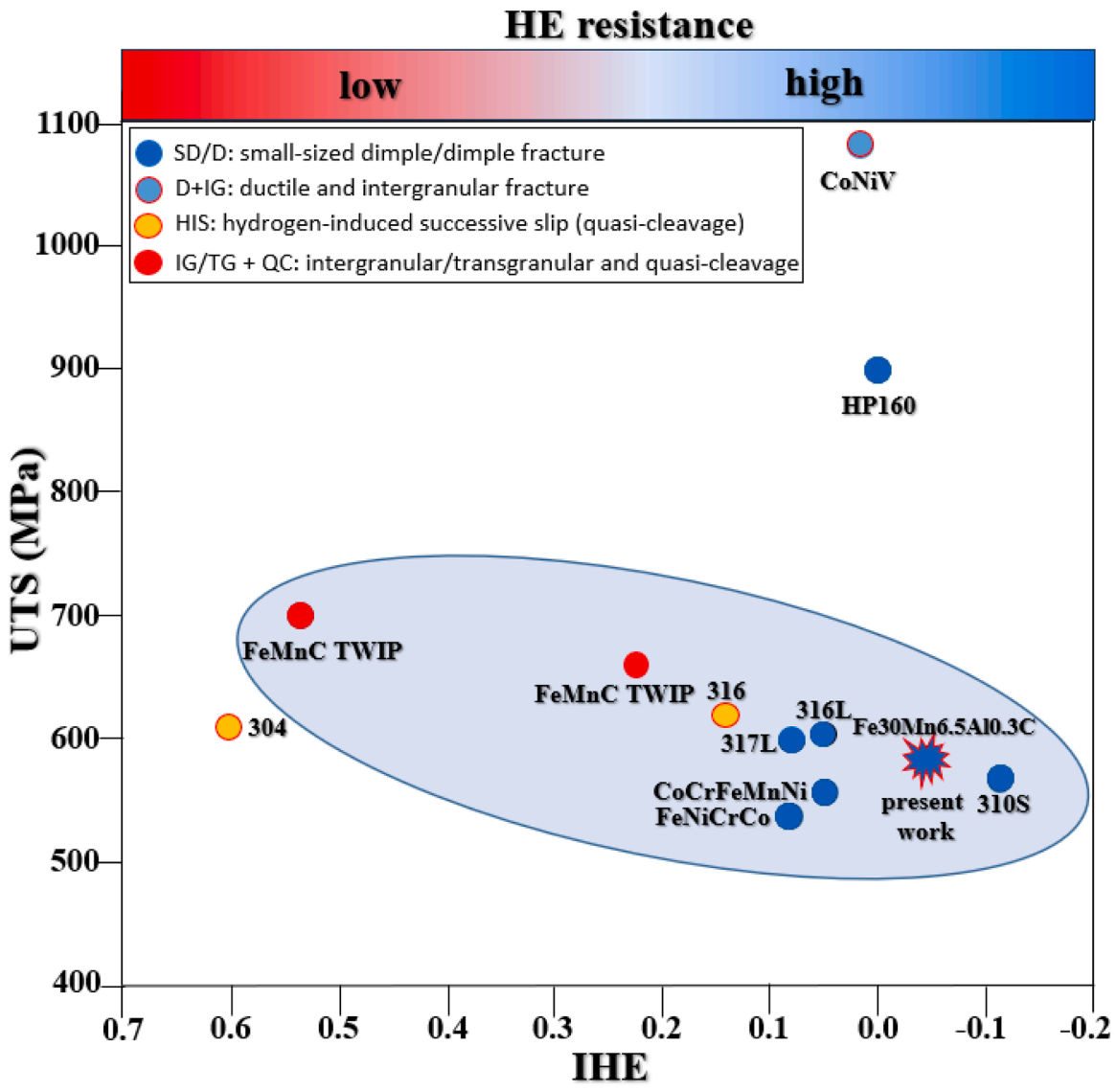

Figure 19. IHE (index of hydrogen embrittlement) vs. ultimate tensile strength (UTS) chart for several austenitic steels and multicomponent alloys tested under gaseous hydrogen charging conditions. The data are summarized in Table 2.

channeling contrast imaging (ECCI), electron backscatter diffraction (EBSD), and scanning transmission electron microscopy (STEM). The contribution of the hydrogen-induced dislocation structure to the hydrogen embrittlement (HE) resistance was analyzed. The following conclusions can be drawn:

- Hydrogen has a small influence on dislocation cells (cell size refinement of ~ 10%) while enhancing the formation of dense dislocation walls. These findings indicate that the influence of hydrogen on the stabilization of primary dislocation configurations with reduced dislocation spacing is comparatively stronger than dislocation trapping by incidental boundaries induced by hydrogen.
- Hydrogen enhances the formation of dislocation structures associated with inhomogeneous plasticity (deformation bands) and strain localization (microbands), resulting in hydrogen-enhanced deformation banding (HEDB) and hydrogen-enhanced microbanding (HEMB) deformation mechanisms. Diffraction analysis confirms the absence of ordered κ-carbides, which indicates that these deformation mechanisms are ascribed to hydrogen-induced effects on plasticity.
- HEDB is associated with specific hydrogen-induced effects on slip bands that promote the formation of two types of deformation bands (DBs), namely, macroscopic kink-bands in grains oriented close to <0 0 1>//TA directions and submicron DBs with intense strain localization formed in grains oriented close to <1 1 1>//TA directions. HEMB is ascribed to hydrogen-induced shear localization generated in two distinguishable microstructural locations: the GNB structure of cell blocks and localized regions of the grain interior associated with DBs. The underlying hydrogen-induced microband nucleation mechanisms were identified.
- The present Fe30Mn6.5Al0.3C low-density steel exhibits a high HE resistance associated with a moderated increase in strength (yield stress increase of 10%) and ductility (increase in the elongation to fracture of ~ 8%). Analysis of the fracture mechanisms and the hydrogen-induced dislocation structures indicate that HEMB influences the deformation behavior of strain localization gradients associated with DBs by promoting the plastic relaxation of DBs and the storage of geometrically necessary dislocations. These effects mitigate the activation of damage mechanisms associated with strain localization gradients and enhance the strain-hardening capacity,

Table 2
Summary of hydrogen-induced effects on the HE susceptibility index (IHE), and fracture mechanisms on fcc alloys and steels exposed at gaseous hydrogen charging conditions. IG: Intergranular fracture; TG: Transgranular fracture; QC: Quasi-cleavage fracture; HIS: Hydrogen-induced slip localization; D: Dimple-containing surface fracture; SD: Small dimple-containing fracture surface; HEDT: hydrogen-enhanced densified twinning; HEMB: Hydrogen-enhanced microbanding.

Alloy composition (wt.%)	Hydrogen content (wt. ppm)	IHE	Fracture mechanisms	Refs.
Fe-18Ni-8Cr (304)	83	0.6	HIS	[55]
Fe-33Mn-1.1C	44	0.53	IG+QC	[82]
Fe-12Mn-1C	——	0.22	IG+TG	[83]
Fe-16Cr-10Ni-2Mo-1Mn (316)	97	0.14	HIS	[55]
25Fe-25Ni-25Cr-25Co HEA	54.3	0.08 (HEDT)	D	[86]
CoCrFeMnNi HEA	76.5	0.05 (HEDT)	D	[34]
33Co33Ni33V MEA	78.2	0.03 (HEDT)	D+IGC	[32]
Fe-17.5Cr-12Ni-2Mo (316L)	33	0.05	SD	[84]
Fe-17.6Cr-12Ni-2Mo (316L)	97	0.05	SD	[55]
Fe-20.7Cr-9.7Ni-4Mn-2Mo (HP160)	97	0	SD	[55]
Fe-18Cr-12.5Ni (317L)	——	0.08	SD	[83]
Fe-24Cr-19.1Ni-1Mn (310S)	133	-0.11 (HEDT)	DS	[87]
63.2Fe-30Mn-6.5Al-0.3C	104	-0.045 (HEMB)	SD	Current work

contributing to the high HE resistance of the steel that is comparable to that of high HE-resistant fcc alloys and steels.

CRediT authorship contribution statement

Ivan Gutierrez-Urrutia: Writing – review & editing, Writing – original draft, Investigation, Formal analysis, Conceptualization. **Yuhei Ogawa:** Writing – review & editing, Data curation. **Akinobu Shibata:** Writing – review & editing, Conceptualization.

Declaration of competing interest

The authors declare that they have no known competing financial interests or personal relationships that could have appeared to influence the work reported in this paper.

Acknowledgments

The authors would like to thank Dr. Singh and Mrs. Nakamura for their support with STEM sample preparation and STEM operation.

References

[1] I. Gutierrez-Urrutia, Low Density Fe–Mn–Al–C Steels, Phase Structures, Mechanisms and Properties, ISIJ Int. 61 (2021) 16–25.
[2] M. Koyama, T. Sawaguchi, K. Tsuzaki, Overview of Dynamic Strain Aging and Associated Phenomena in Fe–Mn–C Austenitic Steels, ISIJ Int 58 (2018) 1383–1395.
[3] K.-G. Chin, C.-Y. Kang, S.Y. Sin, S. Hong, S. Lee, H.-S. Kim, K.-H. Kim, N.J. Kim, Effect of Al addition on deformation and fracture mechanisms in two high manganese TWIP steels, Mater. Sci. Eng. A 528 (2011) 2922–2928.
[4] M. Koyama, E. Akiyama, T. Sawaguchi, D. Raabe, K. Tsuzaki, Hydrogen-induced cracking at grain and twin boundaries in an Fe–Mn–C austenitic steel, Scripta Mater 66 (2012) 459–462.
[5] M. Koyama, E. Akiyama, K. Tsuzaki, Hydrogen embrittlement in a Fe-Mn-C ternary twinning-induced plasticity steel, Corrosion Science 54 (2012) 1–4.
[6] E.J. Song, H.K.D.H. Bhadeshia, D.-W. Suh, Interaction of aluminium with hydrogen in twinning-induced plasticity steel, Scripta Mater 87 (2014) 9–12.
[7] D.K. Han, S.K. Lee, S.J. Noh, S.-K. Kim, D.-W. Suh, Effect of aluminium on hydrogen permeation of high-manganese twinning-induced plasticity steel, Scripta Mater 99 (2015) 45–48.
[8] C. FC, C. CP, L. P, C. SL, Effect of aluminium on TRIP Fe-Mn-Al alloy steels at room temperature, Mater. Sci. Eng. A 160 (1993) 261–270.
[9] Y.S. Chun, J.S. Kim, K.T. Park, Y.K. Lee, C.S. Lee, Mater. Sci. Eng. A 533 (2012) 87–95.
[10] M. Koyama, S. Okazaki, T. Sawaguchi, K. Tsuzaki, Hydrogen Embrittlement Susceptibility of Fe-Mn Binary Alloys with High Mn Content: Effects of table and Metastable e-Martensite, and Mn Concentration, Metall. Mater. Trans. A 47 (2016) 2656–2673.
[11] X.-F. Zhang, Z.-W. Kan, Y. Yang, Y.-X. Wan, J.-X. Li, Z.-Y. Huang, Investigation of the effect of electrolytic hydrogen charging on tensile-ductility loss in different Al-added low density steels, Mater. Sci. Eng. A 795 (2020) 140027.
[12] M.N. Elkot, B. Sun, X. Zhou, D. Ponge, D. Raabe, Hydrogen-assisted decohesion associated with nanosized grain boundary κ-carbides in a high-Mn lightweight steel, Acta Mater 241 (2022) 118392.
[13] V.G. Gavriljuk, V.N. Shivanyuk, J. Foct, Diagnostic experimental results on the hydrogen embrittlement of austenitic steels, Acta Mater 51 (2003) 1293–1305.
[14] D.P. Abraham, C.J. Altstetter, The Effect of Hydrogen on the Yield and Flow Stress of an Austenitic Stainless Steel, Metall. Mater. Trans. A 26 (1995) 2849–2858.
[15] D.G. Ulmer, C.J. Altstetter, Hydrogen-induced strain localization and failure of austenitic stainless steels at high hydrogwn concentrations, Acta Metall. Mater. 39 (1991) 1237–1248.
[16] K.A. Nibur, B.P. Somerday, D.K. Balch, C.S. Marchi, The role of localized deformation in hydrogen-assisted crack propagation in 21Cr-6Ni-9Mn stainless steel, Acta Mater 57 (2009) 3795–3809.
[17] I. Gutierrez-Urrutia, A. Shibata, K. Tsuzaki, Microstructural study of microbands in a Fe-30Mn-6.5Al-0.3C low-density steel deformed at cryogenic temperature by combined electron channeling contrast imaging and electron backscatter diffraction, Acta Mater 233 (2022) 117980.
[18] I. Gutierrez-Urrutia, A. Shibata, Effect of deformation temperature on strain localization phenomena in an austenitic Fe-30Mn-6.5Al-0.3C low-density steel, Acta Mater 264 (2024) 119566.
[19] G. Girardin, C. Huvier, D. Delafosse, X. Feaugas, Correlation between dislocation organization and slip bands: TEM and AFM investigations in hydrogen-containing nickel and nickel-chromium, Acta Mater. 91 (2015) 141–151.
[20] S. Wang, A. Nagao, K. Edalati, Z. Horita, I.M. Robertson, Influence of hydrogen on dislocation self-organization in Ni, Acta Mater 135 (2017) 96–102.
[21] I.M.A. Ghermaoui, A. Oudriss, A. Metsue, R. Milet, K. Madani, X. Feaugas, Multiscale analysis of hydrogen-induced softening in f.c.c. nickel single crystals oriented for multiple-slips: elastic screening effect, Sci. Rep. 9 (2019) 13042.
[22] Q. Sun, J. He, A. Nagao, Y. Ni, S. Wang, Hydrogen-prompted heterogeneous development of dislocation structure in Ni, Acta Mater 246 (2023) 118660.
[23] J.P. Chateau, D. Delafosse, T. Magnin, Numerical simulations of hydrogen–dislocation interactions in fcc stainless steels. Part I: hydrogen–dislocation interactions in bulk crystals, Acta Mater 50 (2002) 1507–1522.
[24] J. Hermida, A. Roviglione, Stacking fault energy decrease in austenitic stainless steels induced by hydrogen pairs formation, Scripta Mater 39 (1998) 1145–1149.
[25] P.J. Ferreira, I.M. Robertson, H.K. Birnbaum, Hydrogen effects on the interaction between dislocations, Acta Mater 46 (1998) 1749–1757.
[26] I.M. Robertson, The effect of hydrogen on dislocation dynamics, Eng. Fract. Mech. 68 (2001) 671–692.
[27] H.K. Birnbaum, P. Sofronis, Hydrogen-enhanced localized plasticity–a mechanism for hydrogen-related fracture, Mater. Sci. Eng. A 176 (1994) 191–202.
[28] G. Girardin, D. Delafosse, Solute-dislocation interactions: modelling and experiments in hydrogenated nickel and nickel base alloys, Mater. Sci. Eng. A 387-389 (2004) 51–54.
[29] M. Wen, S. Fukuyama, K. Yokogawa, Hydrogen-affected cross-slip process in fcc nickel, Phys. Rev. B 69 (2004) 174108.
[30] M. Wen, S. Fukuyama, K. Yokogawa, Cross-slip process in fcc nickel with hydrogen in a stacking fault: An atomistic study using the embedded-atom method, Phys. Rev. B 75 (2007) 144110.
[31] Z.-H. Lai, Y.-T. Lin, Y.-H. Sun, J.-F. Tu, H.-W. Yen, Hydrogen-induced ductilization in a novel austenitic lightweight TWIP steel, Scripta Mater. 213 (2022) 114629.
[32] H. Luo, S.S. Sohn, L.Li Wenjun, X. Li, C.K. Soundararajan, W. Krieger, Z. Li, D. Raabe, A strong and ductile medium-entropy alloy resists hydrogen embrittlement and corrosion, Nature Comm 11 (2020) 3081.
[33] L. Hong, Z. Li, D. Raabe, Hydrogen enhances strength and ductility of an equiatomic high-entropy alloy, Sci. Rep. 7 (2017) 9892.
[34] Y. Zhao, D.-H. Lee, M.-Y. Seok, J.-A. Lee, M.P. Phaniraj, J.-Y. Suh, H.-Y. Ha, J.-Y. Kim, U. Ramamurty, J.-i. Jang, Resistance of CoCrFeMnNi high-entropy alloy to gaseous hydrogen embrittlement, Scripta Mater 135 (2017) 54–58.
[35] T. Zhu, Z.H. Zhong, X.L. Ren, Y.M. Song, F.J. Ye, Q.Q. Wang, A.H.W. Ngan, B. Y. Wang, X.Z. Cao, Q. Xua, Influence of hydrogen behaviors on tensile properties of equiatomic FeCrNiMnCo high-entropy alloy, J. Alloys. Comp. 892 (2021) 162260.
[36] C. Zhang, H. Zhi, S. Antonov, L. Chen, Y. Su, Hydrogen-enhanced densified twinning (HEDT) in a twinning-induce d plasticity (TWIP) steel, Scripta Mater. 190 (2021) 108–112.
[37] I. Gutierrez-Urrutia, S. Zaefferer, D. Raabe, Electron channeling contrast imaging of twins and dislocations in twinning-induced plasticity steels under controlled diffraction conditions in a scanning electron microscope, Scripta Mater 61 (2009) 737–740.

[38] I. Gutierrez-Urrutia, S. Zaefferer, D. Raabe, Coupling of electron channeling with EBSD: toward the quantitative characterization of deformation structures in the SEM, JOM 65 (2013) 1229–1236.
[39] I. Gutierrez-Urrutia, Analysis of FIB induced damage by Electron Channeling Contrast Imaging in the SEM, J. Micros. 265 (2017) 51–59.
[40] E. Nes, Modelling of work hardening and stress saturation in FCC metals, Prog. Mater. Sci. 41 (1998) 129–193.
[41] U.F. Kocks, H. Mecking, Physics and phenomenology of strain hardening: the FCC case, Prog. Mater. Sci. 48 (2003) 171–273.
[42] Q. Liu, N. Hansen, Geometrically necessary boundaries and incidental dislocation boundaries formed during cold deformation, Scripta Metall. Mater. 32 (1995) 1289–1295.
[43] X. Huang, Grain orientation effect on microstructure in tensile strained copper, Scripta Mater 38 (1998) 1697–1703.
[44] D.A. Hughes, N. Hansen, D.J. Bammann, Geometrically necessary boundaries, incidental dislocation boundaries and geometrically necessary dislocations, Scripta Mater 48 (2003) 147–153.
[45] G. Winther, Slip systems extracted from lattice rotations and dislocation structures, Acta Mater 56 (2008) 1919–1932.
[46] B. Hallstedt, A.V. Khvan, B.B. Lindahl, M. Selleby, S. Liu, PrecHiMn-4—A thermodynamic database for high-Mn steels, CALPHAD 56 (2017) 49–57.
[47] K. Higashida, J. Takamura, N. Narita, The Formation of Deformation Bands in f, c. c. Crystals Mater. Sci. Eng. 81 (1986) 239–258.
[48] J.A. Wert, X. Huang, F. Inoko, Deformation bands in a [110]aluminium single crystal strained in tension, Proc. R. Soc. Lond. A 459 (2003) 85–108.
[49] A.J. Schwartz, M. Kumar, B.L. Adams, D.P. Field, Electron Backscatter Diffraction in Materials Science, Springer, 2009.
[50] I.R. Kramer, J.P. Hirth, Effect of hydrogen on the dislocation density distribution, Scripta Metall 18 (1984) 539–541.
[51] M. Dollar, I. Bernstein, The effect of hydrogen on deformation substructure, flow and fracture in a nickel-based single crystal superalloy, Acta Metall 36 (1988) 2369–2376.
[52] D.P. Abraham, C.J. Altsetter, Hydrogen-Enhanced Localization of Plasticity in an Austenitic Stainless Steel, Metall. Mater. Trans. A 26 (1995) 2859–2871.
[53] P.J. Jackson, The role of cross-slip in the plastic deformation of crystals, Mater. Sci. Eng. 57 (1983) 39–47.
[54] P.M. Anderson, J.P. Hirth, J. Lothe, Theory of dislocations, Cambridge University Press, 2017.
[55] O. Takakuwa, J. Yamabe, H. Matsunaga, Y. Furuya, S. Matsuoka, Comprehensive Understanding of Ductility Loss Mechanisms in Various Steels with External and Internal Hydrogen, Metall. Mater. Trans. A 48 (2017) 5717–5732.
[56] C.S. Marchi, T. Michler, K.A. Nibur, B.P. Somerday, On the physical differences between tensile testing of type 304 and 316 austenitic stainless steels with internal hydrogen and in external hydrogen, Int. J. Hydrogen Energy 35 (2010) 9736–9745.
[57] C.S. Marchi, B.P. Somerday, X. Tang, G.H. Schiroky, Effects of alloy composition and strain hardening on tensile fracture of hydrogen precharged type 316 stainless steels, Int. J. Hydrogen Energy 33 (2008) 889–894.
[58] K.A. Nibur, D.F. Bahr, B.P. Somerday, Hydrogen effects on dislocation activity in austenitic stainless steel, Acta Mater 54 (2006) 2677–2684.
[59] O. Takakuwa, Y. Mano, H. Soyama, Increase in the local yield stress near the surface of austenitic stainless steel due to invasion by hydrogen, Int. J. Hydrogen Energy 39 (2014) 6095–6103.
[60] K. Wada, J. Yamabe, H. Matsunaga, Mechanism of hydrogen-induced hardening in pure nickel and a copper-nickel alloy analyzed by micro Vickers hardness testing, Mater. Sci. Eng. A 805 (2021) 140580.
[61] K. Wada, J. Yamabe, Y. Ogawa, O. Takakuwa, T. Iijima, H. Matsunaga, Comparative study of hydrogen-induced intergranular fracture behavior in Ni and Cu–Ni alloy at ambient and cryogenic temperatures, Mater. Sci. Eng. A 766 (2019) 138349.
[62] D.M. Symons, Hydrogen Embrittlement of Ni-Cr-Fe Alloys, Metall. Mater. Trans. A 28 (1997) 655–663.
[63] K. Ichii, M. Koyama, C.C. Tasan, K. Tsuzaki, Comparative study of hydrogen embrittlement in stable and metastable high-entropy alloys, Scripta Mater 150 (2018) 74–77.
[64] Y. Ogawa, O. Takakuwa, K. Tsuzaki, Solid-solution hardening by hydrogen in Fe–Cr–Ni-based austenitic steel: Temperature and strain rate effects, Mater. Sci. Eng. A 879 (2023) 145281.
[65] Y. Guo, T.B. Britton, A.J. Wilkinson, Slip band–grain boundary interactions in commercial-purity titanium, Acta Mater 76 (2014) 1–12.
[66] Q. Luan, H. Xing, J. Zhang, J. Jiang, Experimental and crystal plasticity study on deformation bands in single crystal and multi-crystal pure aluminium, Acta Mater 183 (2020) 78–92.
[67] W. McInteer, A. Thompson, I. Bernstein, The effect of hydrogen on the slip character of nickel, Acta Metall 28 (1980) 887–894.
[68] D.A. Hughes, W.D. Nix, Strain Hardening and Substructural Evolution in Ni-Co Solid Solutions at Large Strains, Mater. Sci. Eng. A 122 (1989) 153–172.
[69] D.A. Hughes, Microstructural evolution in a non-cell forming metal: Al-Mg, Acta Metall. Mater. 41 (1993) 1421–1430.
[70] G. Hachet, J. Li, A.M. Hallil, A. Metsue, A. Oudriss, J. Bouhattate, X. Feaugas, A multi-scale analysis of the different interactions between defects and hydrogen: a review on the contribution of the elastic fields, Eng. Fract. Mech. 218 (2019) 10662.
[71] S. Taketomi, R. Matsumoto, N. Miyazaki, Atomistic study of hydrogen distribution and diffusion around a {112}<111>edge dislocation in alpha iron, Acta Mater 56 (2008) 3761–3769.
[72] A. Oudriss, F. Martin, J. Creus, J. Bouhattate, L. Marchetti, X. Feaugas, Contributions of polarized dislocation walls, internal stresses and vacancies on hydrogen trapping processes in tensile strengthening (100) nickel single crystal, Acta Mater 245 (2023) 118622.
[73] P.J. Jackson, Dislocation modelling of shear in F.C.C. crystals, Prog. Mater. Sci. 29 (1985) 139–175.
[74] P.J. Jackson, The formation of microbands by cross-slip, Scripta Metall 17 (1983) 199–202.
[75] J.C. Huang, G.T. Gray III, Microband formation in shock-loaded and quasi-statically deformed metals, Acta Metall 37 (1989) 3335–3347.
[76] O.L.D. Lange, P.J. Jackson, P.D.K. Nathanson, Stresses and secondary slip between overlapping groups of dislocations, Acta Metall 28 (1980) 833–839.
[77] Z.Q. Wang, I.J. Beyerlein, R. LeSar, Slip band formation and mobile dislocation density generation in high rate deformation of single fcc crystals, Phil. Mag. 88 (2008) 1321–1343.
[78] I.M. Robertson, H.K. Birnbaum, P. Sofronis, Hydrogen Effects on Plasticity, in: J.P. Hirth, L. Kubin (Eds.), Dislocations in Solids. Volume 15, Elsevier Science (2009).
[79] G. Girardin, D. Delafosse, Measurement of the saturated dislocation pinning force in hydrogenated nickel and nickel base alloys, Scripta Mater 51 (2004) 1177–1181.
[80] I. Gutierrez-Urrutia, D. Raabe, Microbanding mechanism in a Fe-22Mn-0.6C (wt.%) high-Mn twinning induced plasticity steel, Scripta Mater 69 (2013) 53–56.
[81] N. Zhao, Q. Zhao, Y. He, R. Liu, W. Zheng, W. Liu, Y. Zhang, Investigation on hydrogen embrittlement susceptibility in martensitic steels with 1000 MPa yield strength, J. Mater. Res. Tech. 15 (2021) 6883–6900.
[82] I.B. Tugluca, M. Koyama, B. Bal, D. Canadinc, E. Akiyama, K. Tsuzaki, High-concentration carbon assists plasticity-driven hydrogen embrittlement in a Fe-high Mn steel with a relatively high stacking fault energy, Mater. Sci. Eng. A 717 (2018) 78–84.
[83] T. Michler, C.S. Marchi, J. Naumann, S. Weber, M. Martin, Hydrogen environment embrittlement of stable austenitic steels, Inter. J. Hyd. Ener. 37 (2012) 16231–16246.
[84] M. Hatano, M. Fujinami, K. Arai, H. Fujii, M. Nagumo, Hydrogen embrittlement of austenitic stainless steels revealed by deformation microstructures and strain-induced creation of vacancies, Acta Mater 67 (2014) 342–353.
[85] X. Zhou, A. Tehranchi, W.A. Curtin, Mechanism and Prediction of Hydrogen Embrittlement in fcc Stainless Steels and High Entropy Alloys, Phys. Rev. Lett. 127 (2021) 175501.
[86] M. Koyama, H. Wang, V.K. Verma, K. Tsuzaki, E. Akiyama, Effects of Mn Content and Grain Size on Hydrogen Embrittlement Susceptibility of Face-Centered Cubic High-Entropy Alloys, Metall. Mater. Trans. A 51 (2020) 5612–5616.
[87] Y. Ogawa, H. Hosoi, K. Tsuzaki, T. Redarce, O. Takakuwa, H. Matsunaga, Hydrogen, as an alloying element, enables a greater strength-ductility balance in a Fe-Cr-Ni-based, stable austenitic stainless steel, Acta Mater 199 (2020) 181–192.